

EARLY-TYPE GALAXIES AT INTERMEDIATE REDSHIFT OBSERVED WITH *HUBBLE SPACE TELESCOPE* WFC3: PERSPECTIVES ON RECENT STAR FORMATION

MICHAEL J. RUTKOWSKI¹, HYUNJIN JEONG², SETH H. COHEN³, SUGATA KAVIRAJ^{4,5}, ROGIER A. WINDHORST³,
RUSSELL E. RYAN, JR.⁶, ANTON KOEKEMOER⁶, SUKYOUNG K. YI², NIMISH P. HATHI⁷, AND MICHAEL A. DOPITA^{8,9,10}

¹ Minnesota Institute for Astrophysics, University of Minnesota, 116 Church Street SE, Minneapolis, MN 55455, USA

² Department of Astronomy, Yonsei University 134, Shinchon-dong, Sudaemun-gu, Seoul 120-179, Korea

³ School of Earth and Space Exploration, Arizona State University, Tempe, AZ 85287-1404, USA

⁴ Centre for Astrophysics Research, University of Hertfordshire, College Lane, Hatfield AL10 9AB, UK

⁵ Department of Physics, University of Oxford, Keble Road, Oxford OX1 3RH, UK

⁶ Space Telescope Science Institute, Baltimore, MD 21218, USA

⁷ Aix Marseille Université, CNRS, LAM, UMR 7326, F-13388, Marseille, France

⁸ Research School of Physics and Astronomy, The Australian National University, Canberra, ACT 2611, Australia

⁹ Astronomy Department, King Abdulaziz University, PO Box 80203, Jeddah, Saudi Arabia

¹⁰ Institute for Astronomy, University of Hawaii, Honolulu, HI 96822, USA

Received 2013 December 28; accepted 2014 September 23; published 2014 November 12

ABSTRACT

We present an analysis of the stellar populations of 102 visually selected early-type galaxies (ETGs) with spectroscopic redshifts ($0.35 \lesssim z \lesssim 1.5$) from observations in the Early Release Science program with the Wide Field Camera 3 (WFC3) on the *Hubble Space Telescope* (*HST*). We fit one- and two-component synthetic stellar models to the ETGs UV-optical-near-IR spectral energy distributions and find that a large fraction ($\sim 40\%$) are likely to have experienced a minor ($f_{YC} \lesssim 10\%$ of stellar mass) burst of recent ($t_{YC} \lesssim 1$ Gyr) star formation. The measured age and mass fraction of the young stellar populations do not strongly trend with measurements of galaxy morphology. We note that massive ($M > 10^{10.5} M_{\odot}$) recent star-forming ETGs appear to have larger sizes. Furthermore, high-mass, quiescent ETGs identified with likely companions populate a distinct region in the size–mass parameter space, in comparison with the distribution of massive ETGs with evidence of recent star formation (RSF). We conclude that both mechanisms of quenching star formation in disk-like ETGs and (gas-rich, minor) merger activity contribute to the formation of young stars and the size–mass evolution of intermediate redshift ETGs. The number of ETGs for which we have both *HST* WFC3 panchromatic (especially UV) imaging and spectroscopically confirmed redshifts is relatively small, therefore, a conclusion about the *relative* roles of both of these mechanisms remains an open question.

Key words: galaxies: elliptical and lenticular, cD – galaxies: evolution – galaxies: star formation – ultraviolet: galaxies

Online-only material: color figures

1. INTRODUCTION

Massive ($M \gtrsim 10^{11} M_{\odot}$) early-type galaxies (ETGs) dominate the stellar mass and baryon budget in the low to intermediate-redshift universe ($z \lesssim 1$; see e.g., Fukugita et al. 1998). However, their assembly and evolution is not yet fully understood and is the subject of active research. Generally, ETGs are observed to form a tight red-sequence in optical color–magnitude space and have long been considered “red and dead” (deVaucouleurs 1961; Kennicutt et al. 1998). Furthermore, ETGs are tightly correlated on the fundamental plane (Bender et al. 1992), and relatively enriched in α -elements (e.g., Mg, Ne; see Trager et al. 1998, 2000; Thomas et al. 2005). This evidence has long been interpreted as support for a common formation scenario (Larson 1974; Pipino & Matteucci 2004; Chiosi & Carraro 2002), in which massive ETGs formed the majority of their stellar mass at high redshift ($z \gg 1$) in a relatively short burst of star formation (Matteucci et al. 1994; Thomas et al. 1999; Faber et al. 2007). This evolutionary history contrasts with the more continuous star formation histories observed for later-type galaxies.

Recently, observations have revised the traditional picture of ETG formation and evolution. Rest-frame far- and near-ultraviolet (FUV and NUV) observations—which are uniquely sensitive to recent star formation in quiescent ETGs (Yi

et al. 2005)—have confirmed that many ($\sim 30\%$) low redshift ($z < 0.3$) ETGs possess $\ll 5\%$ – 10% of their total stellar mass in young stellar populations (Ferreras & Silk 2000; Kaviraj et al. 2007, 2008, 2011). The presence of young stars drives the optically red quiescent galaxies toward (perhaps repeatedly) the green valley (Wyder et al. 2007; Schiminovich et al. 2007), a region bounded in UV–optical color–magnitude—star formation rate (sSFR) parameter space by the traditional blue cloud (rest-frame $(\text{NUV} - r') \simeq 2$ mag; average $\langle \text{sSFR} \rangle \simeq 10^{8-9} \text{ yr}^{-1}$), and the red sequence ($(\text{NUV} - r') \gtrsim 5$ mag; average $\langle \text{sSFR} \rangle \simeq 10^{10-12} \text{ yr}^{-1}$; see, e.g., Mostek et al. 2013; Barro et al. 2013). The fuel for this star formation may be supplied via cold-gas accretion (Lucero & Young 2007; Serra et al. 2012) and/or mergers (Naab et al. 2009; Dekel et al. 2009; Kaviraj et al. 2013a), the latter being ubiquitous in the Λ CDM paradigm of hierarchical galaxy assembly (Eliche-Moral et al. 2010; Khochfar and Burkert 2003). The rate of major mergers is too low at intermediate redshift, thus if RSF is driven by mergers, they are likely to be minor (i.e., with mass ratios, $\mu \gtrsim 1:4$; see López-Sanjuan 2010, 2012; Kaviraj 2014a, 2014b).

High spatial resolution imaging has also confirmed that high-redshift ($z \sim 2$) ETGs are systematically more compact (i.e., higher stellar density and smaller effective radii) than ETGs in the local universe (Daddi et al. 2005; Cassatta et al. 2011,

2013; Trujillo et al. 2006; van Dokkum et al. 2008; Damjanov et al. 2009). In simulations, optimal size–mass growth in ETGs by mass accretion is accomplished via dry (i.e., gas-free; see Naab et al. 2009) minor mergers. Yet dry minor mergers, by definition, do not introduce the cold gas that is necessary for star formation. If minor mergers underpin both the observed size evolution of compact ETGs and recent star formation (RSF), the apparent implication is that the evolution of ETGs is finely tuned—too few wet mergers in cosmological simulations and the observed frequency of recent, minor star formation is difficult to explain; too few dry mergers, and the observed size growth is not achieved. It has been recently pointed out that gas-poor minor mergers are not precluded from growing ETGs to their observed sizes in the local universe, but such mergers cannot yield more than $\sim 4\%$ of the total stellar mass in young stellar populations (Sonnenfeld et al. 2014).

To alleviate the tension surrounding the role of mergers, the loss of baryonic mass by winds has been implicated to explain the observed size–mass evolution (Fan et al. 2008, 2010; Damjanov et al. 2009), although this mechanism remains controversial (see, e.g., Ragone-Figueroa & Granato 2011). Alternatively, many have considered the possibility that a progenitor bias affects the selection of massive ETGs at high redshift for study, thus biasing the measurement of the size–mass evolution for quiescent, compact ETGs (Scarlata et al. 2007; Poggianti et al. 2013; Cassata et al. 2013). Recently, Carollo et al. (2013) extended such a study to include the COSMOS survey (Scoville et al. 2007) and concluded that the introduction of systematically larger quenched ETGs—the progenitors of which were once star-forming disk galaxies—dominate the observed size–mass evolution of ETGs since $z \sim 1$.

Thus, morphologically selected ETGs in the green valley are likely to be either quiescent ETGs that have moved *away* from the red sequence due to the formation of young stars via mergers/cold-gas accretion *or* recently quenched, formerly disk-dominated that are moving *toward* and will eventually transition to red sequence. Without *HST*'s high spatial resolution and the UV sensitivity of the WFC3, it is difficult to study recent star formation and mechanism(s) by which massive galaxies at intermediate redshift ($z \gtrsim 0.5$) can evolve with respect to the green valley. At this redshift range, minor merger remnants and stellar clusters are unresolved or undetected (Peirani et al. 2010; Salim et al. 2012, respectively),¹¹ and the rest-frame FUV and NUV is not observed with SDSS & *GALEX*. In Rutkowski et al. (2012) we presented observations of ~ 100 intermediate redshift ($0.35 < z < 1.5$) ETGs made with the *Hubble Space Telescope* (*HST*) Wide Field Camera 3 (WFC3) as part of the Early Release Science (ERS) program (Windhorst et al. 2011). The ETGs' rest-frame UV–optical colors suggested that a large fraction of these ETGs have likely undergone a minor burst of recent ($t \lesssim 1$ Gyr) star formation. Here, we extend this work by measuring the characteristics of the young and old stellar populations, taking a more general approach to investigate how these ETGs may have approached the intermediate-redshift green valley.

The outline of the paper is as follows. In Section 2, we briefly describe the selection criteria (Rutkowski et al. 2012) used to define the ETG sample. In Section 3, we present constraints on the age and mass of the young and old stellar populations derived from the 0.1–2.0 μm SED of each ETG. We measure the Sérsic profile and the number of likely compan-

ions for each ETG in Section 4, taking advantage of the superior spatial resolution, stable PSF, and low sky-background at UV-optical, near-IR wavelengths of the *HST* WFC3 UVIS/IR and ACS. In Section 5, we investigate correlations between these quantitative morphological parameters and the age and mass fraction of the best-fit young stellar populations. Throughout this paper, we assume a Λ CDM cosmology with $\Omega_m = 0.27$, $\Omega_\Lambda = 0.73$, and $H_0 = 70 \text{ km s}^{-1} \text{ Mpc}^{-1}$ (Komatsu et al. 2011). We use the following *HST* filter designations: F225W, F275W, F336W, F435W, F606W, F775W, F850LP, F098M, F125W, and F160W represent the *HST* WFC3 and ACS filters. FUV and NUV represent the *GALEX* 150 and 250 nm filters, respectively (Morrissey et al. 2005). We quote all fluxes on the AB-magnitude system throughout (Oke & Gunn 1983).

2. OBSERVATIONS AND DATA

Near-UV and near-IR observations were acquired as part of the WFC3 ERS program (HST Program ID #11359, PI: R. W. O'Connell), a 104 orbit medium-depth survey using the *HST* WFC3 UVIS and IR cameras (see Windhorst et al. 2011, for full details). The ERS program observed $\sim 50 \text{ arcmin}^2$ in the Great Observatories Origins Deep Survey-South (GOODS-S) field (Dickinson et al. 2003; Giavalisco et al. 2004) with the *HST* WFC3 UVIS in three filters (F225W, F275W, F336W) and $\sim 40 \text{ arcmin}^2$ with the WFC3 IR in three filters (F098M, F125W, F160W). We prepared mosaic images for all UVIS and IR filters drizzled to a pixel scale of $0''.090 \text{ pixel}^{-1}$. We rebinned the existing ACS images (F435W, F606W, F775Ws, and F850LP) to match the pixel scale of the ERS mosaics.

We will use the ETG catalog identified in Rutkowski et al. (2012) throughout the following analysis. This criteria selected ETGs that have:

1. been imaged in all UV and IR bands to a uniform depth in the ERS field;
2. a spectroscopically confirmed redshift measured in the range $0.35 \lesssim z \lesssim 1.5$;
3. a visual morphology characterized by a centrally peaked light profile, which declines sharply with radius; a high degree of azimuthal symmetry; and a lack of visible internal structure, which is characteristic of ETGs.

Applying these selection criteria to the WFC3 ERS field, we identified 102 ETGs.

In this analysis, we will use the panchromatic (10-filter) photometry for each ETG as measured in Rutkowski et al. (2012). This measured photometry for the ETGs was obtained with a *Source Extractor* (hereafter *SExtractor*; Bertin & Arnouts 1996) in dual-image mode, using the F160W image mosaic as the detection image. Previously, we determined 90% recovery limits for simulated bulge profiles with a half-light radius of $1''.0$ equal to F225W $\lesssim 26.5$, F275W $\lesssim 26.6$, F336W $\lesssim 26.4$, and F435W $\lesssim 26.7$ mag, respectively. We interpret ETGs with magnitudes fainter than these recovery limits as 1σ upper limits. We refer the reader to Rutkowski et al. (2012) for the complete photometry tables and details regarding the selection and classification of the catalog ETGs.

3. CHARACTERIZING THE STELLAR POPULATIONS

3.1. Single-component SED Analysis

The mean rest-frame optical ($g' - r'$) colors and optical (M'_i) absolute magnitudes measured for the majority ($> 75\%$) of ETGs in Rutkowski et al. (2012) are in general agreement with the

¹¹ The *GALEX* point-spread function FWHM $\sim 5''.0$, in comparison to *HST* WFC3 UVIS PSF FWHM $\sim 0''.1$.

optical colors observed for low-redshift red-sequence galaxies, provided a small (~ 0.2 mag) color correction is applied to correct for the passive evolution of the stellar population to the redshift range we considered. This suggests that the stellar mass budgets of the ETGs are likely dominated by relatively old, low-mass stellar objects. The traditional paradigm of ETG formation predicts that these stellar populations formed in a short ($t \lesssim 1$ Gyr), massive burst of star formation at high redshift ($z \gtrsim 3$; see Kaviraj et al. 2013b). As a result, we expect that the optical-IR SEDs—the wavelength regime in which stellar light from $t \gg 1$ Gyr populations dominates the spectrum of old galaxies—should be well-described by stellar population synthesis models that assume a comparable star formation history (SFH).

We produced a library of stellar population models composed of Bruzual & Charlot (2003, hereafter, BC03) population synthesis templates to use for characterizing the old stellar populations in these ETGs. Star formation in these models was defined by a single-burst, exponentially declining SFH with the star formation rate, ψ , characterized by $\psi(t) \propto e^{-t/\tau}$. We calculated models for $N = 16$ values of τ , the decay of the star formation history, defined with a logarithmic stepsize of

$$\Delta(\log(\tau[\text{Gyr}])) = \frac{\max(\log(\tau)) - \min(\log(\tau))}{(N - 1)} = 0.28, \quad (1)$$

over the range $-2.0 < \log(\tau[\text{Gyr}]) < 2.0$. The model ages were defined over the range $1 \times 10^8 < t(\text{yr}) < 13.7 \times 10^9$ with a logarithmic step-size of $\log(\Delta t[\text{yr}]) \simeq 0.02$. A Salpeter stellar initial mass function was assumed (see van Dokkum & Conroy 2010) and the metallicity was fixed at solar. We applied the Calzetti et al. (2000) prescription for dust extinction, assuming $0 \lesssim E(B - V) \lesssim 1$ mag characteristic of low-redshift ETG and spheroidal galaxies (Kaviraj et al. 2011).

We fit these models to the broadband observed optical-IR (F435W, F606W, F775W, F850LP, F098M, F125W, F160W) SEDs of each ETG, measuring the best-fit model parameters by minimizing the goodness-of-fit χ^2_ν statistic for each ETG’s observed SED, following the standard formalism of Papovich et al. (2001). Old, low-mass ($M \sim M_\odot$) stellar populations emit predominantly at optical–near-IR wavelengths observed with this filter set, thus (temporarily) excluding the UV ensures that our one-component fitting is largely insensitive to any RSF. In the fitting process, we fix the redshift of each ETG to its spectroscopic redshift (Table 1; Rutkowski et al. 2012). The age of the universe at this redshift was used to set the maximum allowable stellar age in the library of models considered in the analysis of ETGs’ SED. In Figure 1, we present the best-fit mass and age parameter measured from these one-component SED fits. The SEDs of the majority of ETGs in this sample are dominated by a massive, ($M \gtrsim 10^{10} M_\odot$), relatively dust-free, old ($t > 2\text{--}3 \times 10^9$ Gyr) stellar population—in agreement with the traditional paradigm of galaxy assembly for ETGs.

3.2. Modeling Recent Star Formation with Two-component SED Models

By design, the single-component SED analysis in the previous section is sensitive to the majority (by mass) old stellar populations in these ETGs. Here, we aim to better constrain the *complete* SFH, modeling the SEDs by including synthetic stellar templates that describe both the old and young stellar populations. Well-studied lines and broad absorption complexes (e.g., H α ; Ca H and K, Balmer breaks) at optical wavelengths

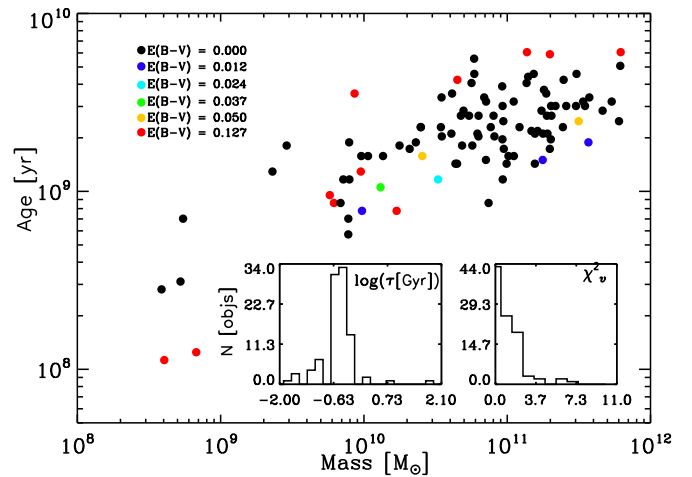


Figure 1. Mass (M_\odot) and age (yr) of the *old* stellar populations of the ETGs, as measured from the best-fit stellar template (Section 3.1). Stellar templates were fit only to the Optical+IR SED (F435W, F606W, F775W, F850LP, F098M, F125W, F160W). In the primary panel, we plot the measured mass-age distribution of ETGs, coded by the best-fit dust extinction $E(B - V)$ assuming a Calzetti et al. (2000) extinction law. Inset in this panel are the distributions of the best-fit τ (the timescale for the exponential decline of the star formation history, see Section 3.1) parameter (left) derived from the SED fits, and reduced χ^2 values for each fit. In general, the majority of ETGs selected here on visual morphology have optical–near-IR SEDs dominated by light from old stellar populations, with little dust, and the majority of star formation likely concluding by $z \gtrsim 2.5$. (A color version of this figure is available in the online journal.)

cannot be used here because only broadband imaging was publicly available for the majority of these ETGs. Enabled by the UV sensitivity of the *HST* we can instead use broadband UV diagnostics to characterize recent ($t \lesssim 1$ Gyr) star formation in these ETGs.

Before characterizing any young stellar population in the ETGs, we must first confirm that the UV emission does not likely arise from old, low-mass ($M \lesssim 1 M_\odot$) stellar populations. Such hot ($T > 25,000$ K) stellar populations (e.g., extreme horizontal branch (EHB) stars, see O’Connell 1999) can produce a “UV Upturn” (UVX). The evolution of the EHB progenitors is not fully understood, but it is believed to be a metallicity-dependent mass-loss effect in old ($t > 10$ Gyr) stars (Yi et al. 1998, 1999).

We apply the UV–optical color–color criteria defined by Yi et al. (2011) to differentiate between UVX-dominated and recently star-forming ETGs. *None* of the ETGs in our sample are found to be dominated at UV–optical wavelengths by the emission from an EHB population. This agrees with the expectation from the theory of the evolution of low-mass stars to the EHB (see Yi et al., 2003), that at $z \gtrsim 0.3$ the UVX will be negligible because the stars in galaxies at this redshift are too young (see Kaviraj et al. 2007). We cannot exclude the possibility of an EHB population, but—if they are present (see Han et al. 2007)—this is a minority stellar population in low-redshift ETGs ($\ll 1\%$ of the total stellar mass, Yi et al. 2011). Where they exist, the blue rest-frame UV–optical colors measured in Rutkowski et al. (2012) likely indicate the presence of a relatively young ($t \lesssim 1$ Gyr) population of massive stars.

The characteristics of any minor, young stellar population in these optically red ETGs will not be well-constrained if the SFHs are modeled with a library of stellar population templates that assumes (Section 3.1) the star formation rate is well-described by a *single*, exponentially declining starburst event from high ($z > 3\text{--}4$) redshift. We extend our analysis of the SFHs to include two-component stellar template models, in which the

Table 1
Measured Characteristics of Catalog ETGs

GOODS ID	Stellar Characteristics			Spatial Characteristics					
	t_{YC} [Gyr]	$f_{YC}/100\%$	χ^2_ν	n	R_e	B/A	θ	m_{F160W}	χ^2_ν
J033202.71-274310.8	0.64 ^{0.078} _{0.000}	0.58 ^{0.420} _{0.240}	7.84	5.78 ± 0.007	10.24 ± 0.023	0.79 ± 0.000	-69.3 ± 0.07	17.18 ± 0.00	1.020
J033203.29-274511.4	0.143 ^{0.059} _{0.053}	0.050 ^{0.030} _{0.024}	1.08				Failed F_{crit}		
J033205.09-274514.0	0.114 ^{0.047} _{0.023}	0.058 ^{0.082} _{0.022}	0.96	2.42 ± 0.086	1.45 ± 0.018	0.92 ± 0.011	27.8 ± 5.62	22.48 ± 0.01	0.441
J033205.13-274351.0	0.114 ^{0.029} _{0.023}	0.094 ^{0.186} _{0.038}	1.21	2.58 ± 0.130	1.08 ± 0.021	0.86 ± 0.007	34.9 ± 2.83	23.61 ± 0.03	0.355
J033206.27-274536.7	0.571 ^{1.929} _{0.443}	0.00 ^{0.290} _{0.000}	1.10	2.55 ± 0.023	2.69 ± 0.008	0.29 ± 0.000	-89.1 ± 0.05	21.95 ± 0.01	0.443
J033206.48-274403.6	0.04 ^{0.208} _{0.047}	0.00 ^{0.006} _{0.000}	0.83	1.25 ± 0.027	2.85 ± 0.017	0.81 ± 0.004	27.6 ± 0.88	21.94 ± 0.01	0.468
J033206.81-274524.3	0.00 ^{0.014} _{0.002}	0.00 ^{0.000} _{0.000}	2.35	2.88 ± 0.148	1.99 ± 0.033	0.34 ± 0.004	-34.0 ± 0.27	22.98 ± 0.03	0.401
J033207.55-274356.6	0.40 ^{0.402} _{0.349}	0.03 ^{0.970} _{0.029}	0.88	4.15 ± 0.064	3.31 ± 0.051	0.85 ± 0.005	-72.6 ± 1.35	21.31 ± 0.01	0.400
J033207.95-274212.1	0.181 ^{0.141} _{0.109}	0.00 ^{0.020} _{0.006}	0.56	3.01 ± 0.098	0.79 ± 0.008	0.55 ± 0.007	68.5 ± 0.67	22.29 ± 0.00	0.526
J033208.41-274231.3	0.40 ^{0.236} _{0.177}	0.01 ^{0.022} _{0.010}	0.34	6.82 ± 0.083	0.60 ± 0.002	0.91 ± 0.003	-17.0 ± 1.33	20.42 ± 0.00	0.721
J033208.45-274145.9	0.00 ^{0.042} _{0.002}	0.00 ^{0.000} _{0.000}	1.04	5.92 ± 0.059	2.15 ± 0.020	0.86 ± 0.003	74.3 ± 0.75	20.21 ± 0.00	0.596
J033208.53-274217.7	0.07 ^{0.089} _{0.050}	0.00 ^{0.003} _{0.001}	1.95	2.87 ± 0.029	3.28 ± 0.012	0.66 ± 0.001	-87.3 ± 0.16	22.03 ± 0.01	0.817
J033208.55-274231.1	0.00 ^{0.078} _{0.002}	0.00 ^{0.002} _{0.000}	1.08	4.26 ± 0.323	3.62 ± 0.264	0.90 ± 0.016	43.8 ± 7.56	24.60 ± 0.05	0.671
J033208.65-274501.8	1.01 ^{0.419} _{0.110}	0.26 ^{0.740} _{0.120}	1.19	1.29 ± 0.016	2.02 ± 0.006	0.63 ± 0.001	-55.7 ± 0.18	21.35 ± 0.01	0.603
J033208.90-274344.3	0.28 ^{0.074} _{0.031}	0.34 ^{0.660} _{0.180}	1.09	1.65 ± 0.058	1.63 ± 0.012	0.62 ± 0.006	-23.8 ± 0.74	24.70 ± 0.01	0.377
J033209.09-274510.8	0.11 ^{0.047} _{0.033}	0.07 ^{0.068} _{0.024}	1.31	1.84 ± 0.255	0.51 ± 0.013	0.40 ± 0.027	17.0 ± 1.964	23.79 ± 0.01	0.368
J033209.19-274225.6	0.571 ^{1.329} _{0.368}	0.02 ^{0.338} _{0.018}	1.02	1.63 ± 0.018	2.82 ± 0.009	0.62 ± 0.001	-34.4 ± 0.18	22.46 ± 0.01	0.551
J033210.04-274333.1	0.00 ^{0.089} _{0.000}	0.00 ^{0.000} _{0.000}	0.86	7.16 ± 0.031	4.25 ± 0.033	0.85 ± 0.002	-76.6 ± 0.38	19.71 ± 0.00	0.556
J033210.12-274333.3	0.227 ^{1.573} _{0.226}	0.00 ^{0.277} _{0.002}	1.42	4.34 ± 0.059	1.41 ± 0.011	0.54 ± 0.003	51.2 ± 0.27	21.26 ± 0.01	
J033210.16-274334.3	0.00 ^{1.699} _{0.000}	0.00 ^{0.089} _{0.000}	0.82	5.17 ± 0.046	2.00 ± 0.017	0.93 ± 0.003	87.6 ± 1.44	20.68 ± 0.01	
J033210.76-274234.6	0.36 ^{0.044} _{0.105}	0.01 ^{0.006} _{0.007}	0.59	1.76 ± 0.002	4.11 ± 0.005	0.73 ± 0.000	77.8 ± 0.10	20.85 ± 0.00	3.786
J033210.86-274441.2	0.143 ^{0.143} _{0.112}	0.00 ^{0.012} _{0.005}	0.24	3.68 ± 0.201	0.94 ± 0.024	0.47 ± 0.007	-73.0 ± 0.69	23.86 ± 0.06	0.442
J033211.21-274533.4	0.05 ^{0.108} _{0.048}	0.00 ^{0.002} _{0.000}	3.67	2.25 ± 0.060	1.34 ± 0.021	0.46 ± 0.002	-30.6 ± 0.15	24.93 ± 0.46	0.439
J033211.61-274554.1	0.02 ^{0.158} _{0.022}	0.00 ^{0.002} _{0.000}	1.77	5.01 ± 0.071	2.40 ± 0.021	0.37 ± 0.002	-55.1 ± 0.15	24.11 ± 0.05	0.407
J033212.20-274530.1	0.36 ^{0.093} _{0.074}	0.02 ^{0.018} _{0.010}	1.06	3.38 ± 0.047	2.81 ± 0.034	0.63 ± 0.004	-26.6 ± 0.43	19.89 ± 0.01	8.33
J033212.31-274527.4	0.36 ^{0.149} _{0.133}	0.02 ^{0.026} _{0.014}	1.28				Fail to Converge		
J033212.47-274224.2	0.45 ^{0.451} _{0.167}	0.03 ^{0.088} _{0.016}	0.75	0.45 ± 0.019	1.97 ± 0.020	0.85 ± 0.007	-14.4 ± 2.16	21.78 ± 0.00	0.637
J033214.26-274254.2	0.181 ^{0.074} _{0.090}	0.02 ^{0.038} _{0.018}	2.37				Failed F_{crit}		
J033214.45-274456.6	0.00 ^{0.250} _{0.004}	0.00 ^{0.013} _{0.000}	1.30	1.81 ± 0.052	3.55 ± 0.055	0.66 ± 0.005	-50.9 ± 0.85	22.09 ± 0.01	0.426
J033214.65-274136.6	0.00 ^{0.019} _{0.000}	0.00 ^{0.000} _{0.000}	0.97	5.73 ± 0.213	4.11 ± 0.101	0.88 ± 0.006	-32.2 ± 2.24	23.00 ± 0.02	0.449
J033214.68-274337.1	0.161 ^{0.066} _{0.047}	0.05 ^{0.086} _{0.030}	2.84	2.64 ± 0.080	1.43 ± 0.013	0.40 ± 0.007	-29.2 ± 0.43	22.31 ± 0.01	0.401
J033214.73-274153.3	0.40 ^{0.236} _{0.118}	0.04 ^{0.058} _{0.018}	0.31	5.40 ± 0.127	0.84 ± 0.010	0.56 ± 0.006	83.2 ± 0.54	21.44 ± 0.00	0.647
J033214.78-274433.1	0.02 ^{0.296} _{0.024}	0.00 ^{0.011} _{0.000}	1.21	1.05 ± 0.030	1.78 ± 0.012	0.70 ± 0.002	-82.2 ± 0.53	23.168 ± 0.02	0.425
J033214.83-274157.1	0.40 ^{0.167} _{0.118}	0.04 ^{0.054} _{0.022}	0.21	0.69 ± 0.017	2.40 ± 0.015	0.88 ± 0.005	-27.2 ± 1.70	22.055 ± 0.00	0.531
J033215.98-274422.9	0.40 ^{0.049} _{0.083}	0.07 ^{0.062} _{0.036}	1.06	3.45 ± 0.057	4.46 ± 0.030	0.55 ± 0.002	64.0 ± 0.19	23.704 ± 0.03	0.413
J033216.19-274423.1	0.28 ^{0.118} _{0.106}	0.02 ^{0.022} _{0.012}	0.39	4.43 ± 0.757	4.11 ± 0.535	0.81 ± 0.033	48.6 ± 6.00	22.920 ± 0.05	4.375
J033217.11-274220.9	0.02 ^{0.006} _{0.016}	1.00 ^{0.000} _{0.996}	3.78				Failed F_{crit}		
J033217.12-274407.7	0.45 ^{0.562} _{0.251}	0.02 ^{0.116} _{0.017}	0.25	2.97 ± 0.109	1.07 ± 0.013	0.31 ± 0.005	-2.6 ± 0.37	23.43 ± 0.03	0.386
J033217.14-274303.3	0.28 ^{0.035} _{0.031}	0.04 ^{0.018} _{0.014}	0.59	4.07 ± 0.019	0.94 ± 0.001	0.87 ± 0.001	-49.8 ± 0.40	19.72 ± 0.00	0.533
J033217.49-274436.7	0.36 ^{0.093} _{0.133}	0.04 ^{0.032} _{0.026}	1.09	8.94 ± 0.100	6.50 ± 0.148	0.99 ± 0.003	-31.1 ± 113.40	20.14 ± 0.01	0.387
J033217.91-274122.7	0.01 ^{0.077} _{0.012}	0.00 ^{0.000} _{0.000}	1.51	2.56 ± 0.041	2.64 ± 0.016	0.93 ± 0.002	-59.3 ± 1.72	22.82 ± 0.01	0.439
J033218.31-274233.5	0.25 ^{0.066} _{0.074}	0.00 ^{0.008} _{0.004}	3.84	5.25 ± 0.014	3.43 ± 0.010	0.48 ± 0.000	-10.9 ± 0.04	19.09 ± 0.00	0.665
J033218.64-274144.4	0.00 ^{0.003} _{0.000}	0.00 ^{0.000} _{0.000}	1.51	3.55 ± 0.605	0.87 ± 0.054	0.76 ± 0.023	-15.1 ± 5.11	23.53 ± 0.04	0.419
J033218.74-274415.8	0.32 ^{0.132} _{0.094}	0.01 ^{0.014} _{0.007}	0.67	2.97 ± 0.029	2.72 ± 0.010	0.58 ± 0.001	61.4 ± 0.12	22.59 ± 0.01	0.450
J033219.02-274242.7	0.07 ^{0.214} _{0.070}	0.00 ^{0.010} _{0.001}	1.50	2.21 ± 0.044	6.06 ± 0.099	0.59 ± 0.005	17.5 ± 0.55	22.87 ± 0.01	0.930
J033219.48-274216.8	0.32 ^{0.132} _{0.118}	0.01 ^{0.012} _{0.009}	0.65	7.93 ± 0.038	2.44 ± 0.015	0.71 ± 0.001	-82.7 ± 0.14	19.29 ± 0.00	0.560
J033219.59-274303.8	0.40 ^{0.105} _{0.083}	0.03 ^{0.028} _{0.016}	1.23	7.64 ± 0.226	2.89 ± 0.039	0.92 ± 0.003	-36.4 ± 1.33	22.05 ± 0.03	0.681
J033219.77-274204.0	0.50 ^{0.925} _{0.505}	0.03 ^{0.966} _{0.033}	0.50				Failed F_{crit}		
J033220.02-274104.2	0.00 ^{0.198} _{0.004}	0.00 ^{0.003} _{0.000}	1.30	9.06 ± 0.130	2.70 ± 0.053	0.89 ± 0.003	-31.4 ± 1.09	20.11 ± 0.01	0.612
J033220.09-274106.7	0.00 ^{0.056} _{0.000}	0.00 ^{0.000} _{0.000}	2.64	9.17 ± 0.147	5.05 ± 0.128	0.62 ± 0.003	-66.0 ± 0.33	20.16 ± 0.01	0.686
J033220.67-274446.4	0.10 ^{0.079} _{0.063}	0.00 ^{0.004} _{0.002}	3.62	3.91 ± 0.026	2.33 ± 0.011	0.60 ± 0.001	-87.8 ± 0.17	20.39 ± 0.00	0.670
J033221.28-274435.6	0.50 ^{0.152} _{0.105}	0.02 ^{0.024} _{0.010}	1.76	0.64 ± 0.004	6.31 ± 0.014	0.49 ± 0.001	-35.1 ± 0.12	20.36 ± 0.00	13.968
J033222.33-274226.5	5.00 ^{1.000} _{4.999}	0.03 ^{0.970} _{0.030}	1.14	3.63 ± 0.050	2.02 ± 0.013	0.43 ± 0.003	60.8 ± 0.20	21.28 ± 0.00	0.421
J033222.58-274141.2	0.571 ^{1.129} _{0.250}	0.03 ^{0.444} _{0.022}	0.20	2.15 ± 0.032	2.53 ± 0.013	0.88 ± 0.003	-85.5 ± 0.93	21.49 ± 0.00	0.666
J033222.58-274152.1	0.25 ^{0.031} _{0.052}	0.74 ^{0.260} _{0.520}	0.84				Failed F_{crit}		
J033223.01-274331.5	0.80 ^{0.094} _{0.520}	0.07 ^{0.924} _{0.064}	0.97	6.13 ± 0.084	2.28 ± 0.031	0.84 ± 0.004	-74.3 ± 0.88	20.84 ± 0.01	0.426

Table 1
(Continued)

GOODS ID	Stellar Characteristics			Spatial Characteristics						
	t_{YC} [Gyr]	$f_{YC}/100\%$	χ^2_v	n	R_e	B/A	θ	m_{F160W}	χ^2_v	
J033224.36-274315.2	0.019 ^{0.003} _{0.014}	1.000 ^{0.000} _{0.988}	9.69							
J033224.98-274101.5	0.102 ^{0.042} _{0.044}	0.006 ^{0.003} _{0.003}	1.80	6.05 ± 0.035	1.82 ± 0.009	0.82 ± 0.001	44.6 ± 0.32	20.03 ± 0.00	5.06	
J033225.11-274425.6	0.031 ^{0.016} _{0.026}	0.009 ^{0.012} _{0.009}	2.11							
J033225.29-274224.2	0.404 ^{0.049} _{0.044}	0.920 ^{0.080} _{0.480}	2.71							
J033225.47-274327.6	0.404 ^{0.167} _{0.044}	0.009 ^{0.014} _{0.202}	3.52	3.74 ± 0.017	5.95 ± 0.022	0.87 ± 0.001	71.2 ± 0.30	21.49 ± 0.00	0.538	
J033225.85-274246.1	0.014 ^{0.041} _{0.013}	0.000 ^{0.001} _{0.000}	1.40							
J033225.97-274312.5	0.453 ^{2.297} _{0.452}	0.009 ^{0.990} _{0.009}	0.36	2.40 ± 0.131	0.82 ± 0.011	0.57 ± 0.011	-33.9 ± 1.22	22.77 ± 0.01	0.443	
J033225.98-274318.9	0.006 ^{0.058} _{0.005}	0.000 ^{0.000} _{0.000}	1.48	6.08 ± 0.129	1.59 ± 0.026	0.44 ± 0.005	-45.2 ± 0.34	21.46 ± 0.01	0.518	
J033226.05-274236.5	5.000 ^{0.000} _{0.750}	1.000 ^{0.000} _{0.400}	2.76	2.31 ± 0.093	2.02 ± 0.029	0.24 ± 0.002	-9.1 ± 0.19	23.05 ± 0.03	0.445	
J033226.71-274340.2	0.321 ^{0.132} _{0.118}	0.012 ^{0.012} _{0.006}	0.36	3.65 ± 0.063	1.35 ± 0.011	0.58 ± 0.002	42.9 ± 0.27	22.65 ± 0.01	0.467	
J033227.18-274416.5	0.571 ^{0.000} _{0.062}	0.120 ^{0.040} _{0.054}	3.69	4.81 ± 0.028	4.17 ± 0.010	0.56 ± 0.000	29.0 ± 0.05	21.16 ± 0.01	1.034	
J033227.62-274144.9	0.203 ^{0.052} _{0.042}	0.018 ^{0.014} _{0.006}	2.75	1.81 ± 0.028	1.85 ± 0.008	0.68 ± 0.002	-44.8 ± 0.28	21.66 ± 0.01	0.640	
J033227.70-274043.7	1.015 ^{0.885} _{0.375}	0.120 ^{0.880} _{0.084}	1.34	4.03 ± 0.078	2.46 ± 0.020	0.33 ± 0.001	-77.0 ± 0.10	22.17 ± 0.02	0.478	
J033227.84-274136.8	0.050 ^{0.153} _{0.047}	0.001 ^{0.007} _{0.000}	1.83	6.75 ± 0.075	10.16 ± 0.21	60.61 ± 0.002	52.7 ± 0.27	20.30 ± 0.01	0.492	
J033227.86-274313.6	0.019 ^{0.062} _{0.016}	0.000 ^{0.005} _{0.000}	1.43							
J033228.88-274129.3	0.203 ^{0.202} _{0.164}	0.003 ^{0.010} _{0.003}	0.64	2.75 ± 0.017	3.28 ± 0.007	0.91 ± 0.001	-56.4 ± 0.59	21.88 ± 0.01	0.542	
J033229.04-274432.2	5.000 ^{0.000} _{0.999}	1.000 ^{0.000} _{1.000}	0.58	2.20 ± 0.096	1.32 ± 0.016	0.20 ± 0.010	-51.3 ± 0.42	22.34 ± 0.00	0.922	
J033229.30-274244.8	0.072 ^{0.089} _{0.052}	0.004 ^{0.009} _{0.003}	0.89	1.25 ± 0.058	2.16 ± 0.022	0.55 ± 0.005	82.7 ± 0.58	22.45 ± 0.01	0.503	
J033229.64-274030.3	0.102 ^{0.101} _{0.062}	0.009 ^{0.026} _{0.006}	2.08	1.32 ± 0.036	2.02 ± 0.013	0.43 ± 0.005	87.3 ± 0.40	22.39 ± 0.00	0.449	
J033230.56-274145.7	0.143 ^{0.059} _{0.042}	0.042 ^{0.046} _{0.020}	1.82	0.95 ± 0.012	1.63 ± 0.005	0.58 ± 0.002	78.4 ± 0.26	21.64 ± 0.00	0.361	
J033231.84-274329.4	0.002 ^{0.225} _{0.001}	0.000 ^{0.009} _{0.000}	0.58	7.66 ± 0.272	3.38 ± 0.164	0.90 ± 0.011	-78.4 ± 3.61	21.71 ± 0.02	0.393	
J033232.34-274345.8	0.114 ^{0.029} _{0.050}	0.040 ^{0.056} _{0.024}	1.58							
J033232.57-274133.8	0.001 ^{0.001} _{0.000}	0.002 ^{0.000} _{0.000}	2.37							
J033232.96-274106.8	0.143 ^{0.037} _{0.016}	0.048 ^{0.026} _{0.014}	0.57	0.78 ± 0.015	1.15 ± 0.005	0.89 ± 0.002	69.8 ± 1.37	23.30 ± 0.02	0.480	
J033233.28-274236.0	5.000 ^{0.000} _{0.999}	0.180 ^{0.820} _{0.180}	0.10	2.59 ± 0.169	1.18 ± 0.023	0.39 ± 0.014	38.6 ± 0.92	23.03 ± 0.01	0.464	
J033233.40-274138.9	0.203 ^{0.084} _{0.089}	0.016 ^{0.026} _{0.010}	2.20	1.87 ± 0.023	2.25 ± 0.007	0.82 ± 0.002	-21.0 ± 0.48	23.37 ± 0.03	0.388	
J033233.87-274357.6	0.005 ^{0.250} _{0.004}	0.000 ^{0.007} _{0.000}	1.48	3.62 ± 0.070	1.13 ± 0.008	0.91 ± 0.005	53.1 ± 2.57	21.53 ± 0.00	0.458	
J033234.34-274350.1	0.161 ^{0.094} _{0.059}	0.009 ^{0.010} _{0.004}	3.56	9.73 ± 0.086	5.43 ± 0.093	0.84 ± 0.002	28.7 ± 0.51	19.77 ± 0.01	0.430	
J033235.10-274410.7	0.052 ^{0.028} _{0.026}	0.012 ^{0.010} _{0.006}	8.73	4.86 ± 0.128	3.17 ± 0.094	0.83 ± 0.009	35.9 ± 1.91	21.44 ± 0.01	0.392	
J033235.63-274310.2	0.001 ^{0.025} _{0.000}	0.000 ^{0.000} _{0.000}	1.16	4.53 ± 0.095	4.08 ± 0.037	0.54 ± 0.002	-24.8 ± 0.22	22.43 ± 0.01	0.439	
J033236.72-274406.4	0.143 ^{0.059} _{0.063}	0.009 ^{0.006} _{0.005}	0.67	3.79 ± 0.086	4.87 ± 0.065	0.54 ± 0.003	23.9 ± 0.28	22.96 ± 0.02	0.403	
J033237.32-274334.3	0.114 ^{0.113} _{0.079}	0.004 ^{0.005} _{0.003}	1.15	1.73 ± 0.020	4.37 ± 0.043	0.87 ± 0.005	-86.8 ± 1.58	21.34 ± 0.01	0.493	
J033237.38-274126.2	0.404 ^{0.167} _{0.149}	0.007 ^{0.012} _{0.005}	1.72							
J033238.06-274128.4	0.128 ^{0.232} _{0.127}	0.001 ^{0.006} _{0.001}	2.32	5.80 ± 0.032	4.76 ± 0.037	0.58 ± 0.001	40.0 ± 0.12	19.67 ± 0.00	0.535	
J033238.36-274128.4	0.286 ^{0.223} _{0.125}	0.050 ^{0.290} _{0.034}	6.48	3.35 ± 0.060	1.21 ± 0.008	0.90 ± 0.004	46.2 ± 2.49	24.37 ± 0.05	0.475	
J033238.44-274019.6	0.026 ^{0.117} _{0.025}	0.000 ^{0.002} _{0.000}	1.14	6.01 ± 0.074	3.09 ± 0.042	0.72 ± 0.003	-80.6 ± 0.45	20.71 ± 0.01	0.442	
J033238.48-274313.8	0.255 ^{0.066} _{0.052}	0.160 ^{0.360} _{0.078}	1.66							
J033239.17-274026.5	0.321 ^{0.083} _{0.066}	0.032 ^{0.030} _{0.014}	1.02	2.41 ± 0.026	3.83 ± 0.014	0.65 ± 0.001	-28.7 ± 0.21	22.85 ± 0.01	0.448	
J033239.17-274257.7	0.571 ^{0.236} _{0.211}	0.032 ^{0.040} _{0.018}	0.54	5.59 ± 0.022	5.30 ± 0.019	0.89 ± 0.000	20.8 ± 0.24	20.47 ± 0.00	0.562	
J033239.18-274329.0	0.003 ^{0.224} _{0.002}	0.000 ^{0.006} _{0.000}	0.44	5.85 ± 0.149	2.55 ± 0.065	0.87 ± 0.008	25.1 ± 2.21	21.81 ± 0.01	0.360	
J033239.52-274117.4	0.052 ^{0.203} _{0.052}	0.000 ^{0.005} _{0.000}	1.42	1.41 ± 0.022	3.57 ± 0.019	0.63 ± 0.003	4.7 ± 0.33	22.26 ± 0.01	0.457	
J033240.38-274338.3	0.025 ^{0.047} _{0.022}	0.000 ^{0.001} _{0.000}	0.65	4.30 ± 0.048	5.68 ± 0.083	0.64 ± 0.003	26.2 ± 0.37	20.90 ± 0.01	0.376	
J033241.63-274151.5	0.038 ^{0.052} _{0.034}	0.000 ^{0.001} _{0.000}	4.30	1.99 ± 0.036	3.70 ± 0.020	0.94 ± 0.004	9.3 ± 2.85	22.70 ± 0.01	0.474	
J033242.36-274238.0	0.509 ^{0.132} _{0.149}	0.018 ^{0.018} _{0.010}	1.51	8.65 ± 0.048	5.77 ± 0.056	0.46 ± 0.000	74.4 ± 0.06	18.79 ± 0.00	0.977	
J033243.93-274232.4	0.001 ^{0.063} _{0.000}	0.000 ^{0.000} _{0.000}	3.03	3.54 ± 0.056	4.84 ± 0.039	0.59 ± 0.001	28.6 ± 0.25	22.49 ± 0.01	0.478	
J033244.97-274309.1	0.009 ^{0.171} _{0.008}	0.000 ^{0.002} _{0.000}	4.93							

Notes. We present spatial and stellar characteristics measured for the ETGs in Sections 3.2 and 4, respectively. Columns 2–4 provide characteristics of the best-fit young stellar population. Uncertainties associated with these parameters represent the 68% confidence interval. Columns 5–10 provide quantitative characteristics of the ETGs morphology. Row values associated with the spatial parameters in these columns are defined as follows: “Failed F_{crit} ” = galaxies that failed the criterion for identifying well-resolved galaxies were not fit (see Section 4.1); “Not Fit” = galaxies were not fit because the light-profiles of the ETG were strongly blended with bright neighbors; “Fail to Converge” = one or more parameters could not be well-fit by GALFIT. The χ^2_v values of ETGs in Column 10 are provided in bold for the ETGs that were better fit with a two-component spatial model (i.e., PSF and Sérsic model, see Section 4.1).

SFH is defined by two independent bursts of star formation of varying mass fractions and ages.

In this analysis we follow the same methodology defined in Jeong et al. (2007). We fit a two-component synthesized

stellar populations model *simultaneously* to the observed ERS photometry, minimizing the χ^2_v of the model fit to measure the best-fit model to each ETG’s ten-filter SED. As in Jeong et al. (2007), we applied a template library of stellar population

models for which the old stellar population is modeled by the Y^2 models that include EHB stars (Yi et al. 2003), assuming an initial burst of star formation at $z \simeq 3$ (Rutkowski et al. 2012; Kaviraj et al. 2013b). The second component is designed to represent any possible young stellar components and is derived from the BC03 templates assuming a fixed solar metallicity for all models. When fitting the complete UV–optical near-IR SED, only the mass of the old stellar population models was variable. In contrast, both the age (hereafter, t_{YC}) and the mass fraction ($f_{YC} = (M_{\text{young}}/M_{\text{total}}) \times 100\%$) of the younger stellar component were variable— $10^{-3} < t_{YC}[\text{Gyr}] < 5$ and $10^{-4} < f_{YC}[\%] < 100$. Both stellar populations components could be derived from the BC03 models in principle because the color–color measurements demonstrate that the contribution from UV-bright, old stellar populations is likely to be negligible.

If the characteristics of the young and old stellar populations are derived from an SED analysis that uses a library of two-component synthesized stellar population templates derived *exclusively* from the BC03 templates, the derived age and mass fraction of the young stellar populations are in good agreement ($\sim 90\%$ of the ETGs agree, to within the measurement uncertainties) with those measured using synthesized BC03 + Y^2 libraries as discussed previously. For the few ETGs, where they exist, we can attribute discrepancies between the best-fit age and mass fraction measured using these two libraries to degeneracies in the fitting arising from the large photometric uncertainties in one or more of the bands that assess rest-frame UV emission (i.e., these ETGs have a signal-to-noise ratio in the UV $\lesssim 1$).¹²

For ease of comparison of these results with similar measurements of the RSF in ETGs at lower redshift, we chose to define the two-component synthesis models used here as identical to Jeong et al. (2007). Note that in this two-component SED analysis we did not apply an explicit correction for dust. Dust preferentially attenuates the SED at UV wavelengths, thus the fraction of ETGs that are found to have experienced a minor, recent star formation event is a *lower* limit to the true fraction.

A representative two-component model fit SED is shown in Figure 2 for ETG J033212.20–274530.1. In Table 1, we present the best-fit parameters from our two-component SED analysis, with upper and lower uncertainties on the measurement of each free parameter indicating the 68% confidence level. Where they exist, large young stellar population parameter uncertainties can be primarily attributed to the *photometric* uncertainties associated with the WFC3 UVIS data. The ERS program is a medium-depth survey that observed these UV-faint ($F225W \gtrsim 23$ mag) ETGs to a signal-to-noise ratio in the range $1 \lesssim S/N \lesssim 20$ (see Table 1 in Rutkowski et al. 2012). These photometric uncertainties are markedly lower¹³ than those measured in previous surveys of comparable galaxies at this intermediate redshift range (e.g., Ferreras & Silk 2000). Although χ^2_{ν} values of the best-fit models are generally small ($\chi^2_{\nu} \lesssim 1-2$), we caution that the uncertainty in the measurement t_{YC} & f_{YC} is not correspondingly small, due to the implicit degeneracies in fitting these models to SEDs with large photometric uncertainties. Furthermore,

¹² For the comparison made here, we produced a library of models derived exclusively from BC03 to those discussed in the text, in which we assume that (1) the majority of the stellar mass in the ETGs was formed in a short ($\tau < 100$ Myr) burst of star formation at high ($z_f \sim 3.5$) redshift, and (2) a secondary, more recent burst ($0.01 < t_{YC}[\text{Gyr}] < 5.0$) with a varying mass fraction ($10^{-3} < f_{YC}[\%] < 100$). In general, the results of fitting two-component models derived from BC03 or BC03 and Y^2 stellar libraries were in very good agreement, as expected.

¹³ This is a testament to the improved UVIS capabilities of the *HST* considering the total exposure time (~ 2 orbits) for the field at UV wavelengths.

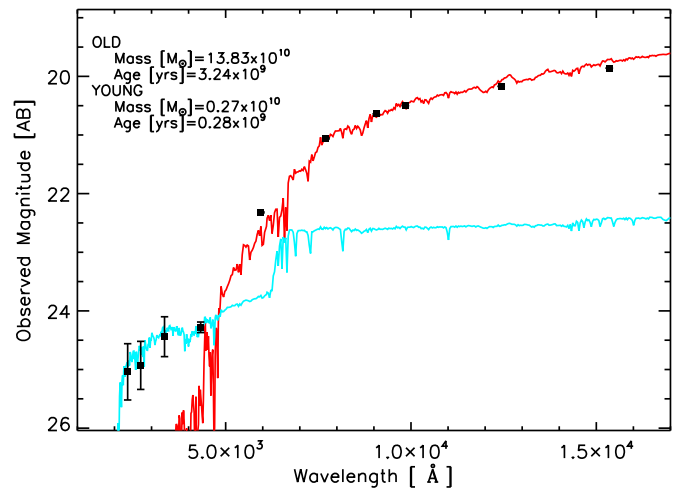


Figure 2. Representative fit of the two-component synthetic stellar population to the 10-band SED measured for a catalog ETG (J033212.20–274530.1). Here, the contribution of the old stellar population, constituting a majority of the stellar mass in this galaxy, is plotted in red. The young stellar component is plotted in blue. Best-fit parameters associated with each stellar population are inset in the figure.

(A color version of this figure is available in the online journal.)

distinguishing between a massive old stellar population and a relatively low-mass young ($t \lesssim 50$ Myr) starburst—in which the UV-light can be strongly attenuated by the young stellar population dusty birth cloud—using broadband photometry alone is difficult (see, e.g., Kaviraj et al. 2007). These systematic effects are more pronounced at the high redshift ($z > 1$), a range in which the observed ERS filters are insensitive to rest-frame wavelengths greater than $\sim 1 \mu\text{m}$, where old stellar populations dominate the SED.

Throughout the text, we will define ETGs to have evidence for recent star formation when the characteristics of the best-fit young stellar population from this two-component SED analysis is in the range of $1 < f_{YC}[\%] < 10$ and $0.1 < t_{YC}[\text{Gyr}] < 1$. Applying this criteria, we conservatively measure *at least* $\sim 40\%$ of ETGs to have experienced a recent, minor burst of star formation in a sample of 77 total ETGs well-fit (i.e., $\chi^2_{\nu} < 2$) with this two-component analysis. The mean age and mass fraction of the best-fit young stellar population component for the sample equals $t_{YC} = 360 \pm 160$ Myr and $f_{YC} = 3.7 \pm 2\%$. At low redshift ($z \lesssim 0.1$), Kaviraj et al. (2007) observed $\sim 30\%$ of ETGs to have UV colors consistent with recent star formation, with the average age of the young stellar component of ~ 300 – 500 Myr. At higher redshift ($1 < z < 3$), Kaviraj et al. (2013a) found that $\sim 60\%$ of massive *spheroidal* galaxies have evidence of recent star formation and have a redshift of formation $z_f \simeq 3$ – 4 . Considering only the *magnitude* of the observed fraction of ETGs with RSF suggests that star formation in ETGs generally declines with decreasing redshift.

Each of these previous measurements of the fraction of ETGs with RSF is a *lower* limit to the total fraction at a given redshift, as the measurements are subject to the photometric completeness in each survey, particularly at the UV wavelengths most sensitive to recent star formation in these optically red ETGs. This completeness can vary considerably between surveys. For example, the *GALEX* Medium Imaging Survey (MIS)—which was used in the measurement of the low-redshift fraction of ETGs with RSF in Kaviraj et al. (2008)—is complete to $\text{NUV} < 23$; our ERS data probes UV magnitudes that are 2.5 mag *fainter*. We measure a fraction of ETGs with RSF

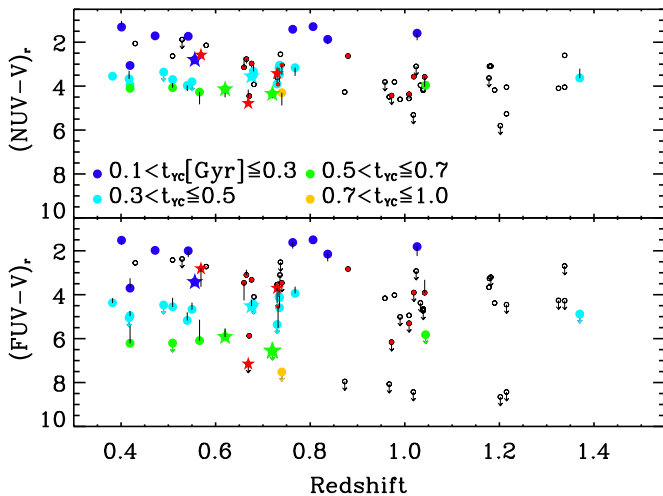


Figure 3. Rest-frame $(\text{NUV}-V)_r$ (top) and $(\text{FUV}-V)_r$ (bottom) colors of the ETGs measured from the best-fit ($\chi^2_\nu < 2$) two-component model (see Section 3.2), plotted with a color scheme indicating the age of the best-fit young stellar component. Large, filled points indicate ETGs meeting conservative requirements defined in Section 3.2 for RSF ($1 < f_{YC} [\%] < 10$; $0.1 < t_{YC} [\text{Gyr}] < 1$). Small, red filled points indicate ETGs consistent with recent star formation, but not meeting conservative criteria for recent star formation (see Section 3.2 for details). Small circles indicate ETGs best-fit with a two-component model consistent with a quiescent star formation history. Throughout, X-ray/radio sources are indicated by star symbols. Overplotted for these data are the offsets between the UV-optical colors derived from the analysis in Section 3.2 and the measured colors, inferred from the *HST* photometry and presented in Rutkowski et al. (2012). These offsets are small ($\Delta \ll 0.3$; for clarity, only offsets larger than 0.2 mag are plotted) indicating the method applied in Rutkowski et al. (2012) to transform observed colors with the *HST* filter set to the rest-frame *GALEX* FUV and NUV optical colors are valid for intermediate redshift ETGs. Data with a small, downward pointing arrow indicate that the UV-optical color of the galaxy was reported as an upper limit in Table 5 of Rutkowski et al. (2012).

(A color version of this figure is available in the online journal.)

that is approximately equal to 30% (11/38 ETGs) and consistent with the measurement in the local universe, if *only* ETGs with $M_r < -21.3$ (see Table 5; Rutkowski et al. 2012) are considered (i.e., including only those galaxies as bright as those considered in the sample of Kaviraj et al. 2008).

In Figure 3 we provide the $(\text{FUV}-V)_r$ and $(\text{NUV}-V)_r$ colors of the ETGs measured from the two-component analysis, plotted with respect to their spectroscopic redshifts. Here, ETGs measured with recent star formation (as defined by the conservative criteria above) are indicated as large, filled colored points, with an inset color scheme corresponding to the best-fit young stellar component. In addition, we include those ETGs (smaller, red filled points) with measurement uncertainties of the age and stellar mass fraction of young stars consistent (i.e., < 1 dex, see Table 1) with recent star formation. Black, unfilled circles in the figure indicate ETGs whose best-fit young stellar parameters are consistent with a quiescent star formation history. In addition to these measured data, we incorporate additional data for a subset of ETGs from the catalogs presented in Rutkowski et al. (2012). We overplot X-ray/Radio sources as filled star symbols, and recently star-forming ETGs with UV-optical colors previously reported as upper limits are overplotted with a small, down(red)ward-pointing arrow. We also overplot (vertical lines) the offset between the UV-optical color reported in Rutkowski et al. (2012) and those measured from the best-fit two-component model. For clarity, we only show the color offset when the difference between the rest-frame colors derived from the broadband transformation in

Rutkowski et al. (2012) and the model colors is greater than 0.2 mag. Few ($\sim 15\%$) ETGs show large offsets—this confirms that the generalized transformation of the observed broadband UV-optical colors to the rest-frame *GALEX* UV-optical colors is reasonable for the majority of intermediate redshift ETGs.

In Figure 3, in particular for the $(\text{FUV}-V)_r$ colors, there appears to be an evolution from high to low redshift toward relatively *bluer* colors. This contradicts the initial conclusion that the sample is consistent with a general decline, or potentially constant, in the fraction of ETGs experiencing recent star formation from $2 < z < 3$ to $z \sim 0$. The trend does not likely represent a cosmological effect. Rather, the eye is strongly biased by the few extremely red ($\text{FUV}-V \gtrsim 7$) ETGs at $z \gtrsim 1$, whose colors were derived from the two-component SED analysis. In this analysis these ETGs are marked by downward-pointing arrows, indicating that these ETGs were non-detected in the rest-frame FUV. Additionally, these galaxies are relatively faint ($m_{F606W} \sim 26$) at optical wavelengths. Uncertainties in the measurement of the best-fit model from which these UV-optical colors are derived are further compounded by the fact that at high redshift ($z > 1$) the reddest ERS filter (F160W) is sensitive to rest-frame optical ($\lambda < 8000 \text{ \AA}$) emission. As a result, at $z \gtrsim 1$ the stellar mass in old stars becomes increasingly difficult to constrain without the near-IR rest-frame data available for the ETGs at lower redshifts. Similarly, the young stellar mass fraction *relative to* the total old stellar mass becomes increasingly difficult to constrain. Thus, for these ETGs—which were measured to have a mass fraction consistent with zero—the derived UV-optical colors will be very red, not for physical reasons but as a result of these compounding photometric and modeling uncertainties. The initial conclusion that the fraction of star-forming ETGs declines or remains constant, as a function of decreasing redshift, remains tenable. We note that the addition of deeper UV photometry and IR rest-frame photometry could improve the uncertainties associated with the higher redshift ETGs’ rest-frame UV-optical measured photometry and stellar population fitting (although existing archival data is at significantly lower spatial resolution).

4. MORPHOLOGICAL ANALYSIS OF ETGS AND THEIR LOCAL ENVIRONMENTS

Feedback from starbursts or AGN (Silk & Rees 1998) in the progenitors of massive ETGs may have expelled or destroyed the fuel necessary for subsequent starbursts (see simulation results from Kaviraj et al. 2007; Schawinski et al. 2009; Kaviraj et al. 2013b). If quiescent ETGs are to form new stars then they must acquire cold gas by accretion and/or minor mergers from the local environment. Alternatively, the quenching of star formation in later-type S0/lenticular galaxies (Kannappan et al. 2009; Lucero & Young 2013) or disk galaxies (e.g., Carollo et al. 2013) could force these galaxies to transition away from the blue-cloud and toward the red-sequence as in situ gas reservoirs are consumed on short ($t \sim 1$ Gyr) timescales (Schawinski et al. 2014).

The high spatial resolution and continuous UV-optical, near-IR coverage of our *HST* WFC3 data allows us to directly search for evidence of the mechanism(s) driving the observed recent star formation. In Section 4.1, we measure Sérsic profiles (Sérsic 1968) of the ETGs to determine the relative fraction with bulge- and disk-like dominated light-profiles. A joint consideration of the quantitative morphologies (Section 4.1) in conjunction with the star formation histories (Section 3.2), and companion analysis (Section 4.2) may provide clues to the mechanism by which ETGs formed young stars. For example, if

a positive correlation exists between the frequency of disk-like light-profiles in association with ETGs in *isolated environments* (i.e., no satellites are observed in these deep UV-optical, near-IR data) in close proximity to the ETG with evidence of RSF, this could implicate the quenching of star formation in (formerly) disk-dominated galaxies as an important mechanism for motivating RSF. If this result exists in conjunction with the measurement of a *negative*, for example, correlation between the frequency of companions and RSF in ETGs, then this could imply that such quenching—in contrast to environmental factors (e.g., mergers)—are relatively *more* important for motivating RSF in intermediate redshift ETGs.

4.1. Quantitative Morphology of ETGs

These ETGs were identified in Rutkowski et al. (2012) by visual selection based on their similarity with the classical morphology of ETGs: a high degree of rotational symmetry and smoothly varying stellar light-profile. Such light-profiles can be well described with relatively few parameters, for example, the Sérsic profile defined as:

$$I(r) = I(0) \times \exp[-b_n(r/r_e)^{1/n}], \quad (2)$$

where $I(0)$ is the intensity at radius $r = 0$, r_e is the half-light radius, n is the Sérsic index, and b_n is a normalization constant that is a function of the Sérsic index and ensures that the radius r_e encloses half of the total galaxy light. Generally, disk-dominated galaxies are described by a Sérsic profile with $n \simeq 1$; bulge-dominated, spheroidal galaxies are best-fit by Sérsic profile with $n \simeq 4$. However, a large dispersion for spheroidals is observed. At low redshift, Kormendy et al. (2009) measured a mean Sérsic index of $n \simeq 3.8$ ($N = 37$ ETGs) with a large spread (>35% of the ETGs were measured $n > 4$; 60% of those were measured with $n > 7$). Krajnovic et al. (2013) measured disk-like Sérsic profiles ($n \lesssim 2$) for the majority of the SAURON sample of local ellipticals (de Zeeuw et al. 2002). High-redshift compact, quiescent ETGs also are found to have a large dispersion in measured Sérsic indices—van der Wel et al. (2011) and Ryan et al. (2012) report $n \lesssim 2$ for 30%–60% of compact ($r_e \lesssim 1$ kpc) massive ($\log(M/M_\odot) \gtrsim 11$) quiescent ETGs, whereas Cassata et al. (2013) and Williams et al. (2014) report large ($n > 2.5$) indices for $\sim 90\%$ of ETGs. Considering the wide range of observed morphologies of ETGs, we can reasonably expect to find a similar diversity in this sample of visually selected ETGs, especially as our sample selection includes S0s/Lenticulars and compact ETGs (see Table 2 in Rutkowski et al. 2012).

A quantitative assessment of the ETGs morphologies may reveal unique clues to the assembly histories of the ETGs. For example, in simulations of gas-rich major mergers at high redshift, Wuyts et al. (2010) found that the ETG descendants of such mergers have surface brightness profiles best characterized by large Sérsic indices ($n \lesssim 10$), with a core, young component associated with the final coalescence of the merger. In our sample, a visual inspection of the rest-frame UV morphologies (see Figure 1 in Rutkowski et al. 2012) reveals that for the $\sim 30\%$ of the ETGs that show appreciable UV emission, this light appears to be dominated by core emission. The combination of the blue UV–optical colors in these ETGs and core-dominated UV light-profiles could, in light of this Wuyts et al. result (and others, see Hopkins et al. 2008, 2009), provide clues about the formation and evolution of the ETGs.

We used GALFIT (Peng et al. 2002) to first measure the best-fit Sérsic profile for each ETG in 200 kpc \times 200 kpc postage

stamp images extracted from the ERS F160W mosaics. We implemented GALFIT via the IDL software wrapper *iGALFIT*¹⁴, which is useful for iterative batch processing. This software requires the user to provide an image and weight map in the same units (counts s^{-1}), ensuring that the uncertainty (χ_ν^2) of each profile fit in GALFIT is properly normalized.

We prepared large (250–500 square pixels) postage stamps for each ETG for analysis with GALFIT. We masked a large ($20 \lesssim N \lesssim 50$) number of regions in each postage stamp that contained neighboring galaxies or noisy pixels (e.g., at WFC3 chip and mosaic gaps). It was never necessary to mask more than $\sim 10\%$ of the total image area, but this masking is necessary. GALFIT calculates the sky brightness locally within each image, and fits the model light-profile assuming that all flux within the region of interest is associated with the ETG. Identifying and removing the contaminating sources (e.g., foreground and background objects) ensures a more accurate measurement of the light-profile.

In Table 2 of Rutkowski et al. (2012), 15 galaxies were noted for their compact morphologies, so it is also necessary to exclude ETGs that may be only marginally spatially resolved. We identify which marginally resolved ETGs to exclude by fitting all ETGs with a Sérsic profile and an empirical PSF (defined by stacking known stars in the ERS field, see Windhorst et al. 2011). We then calculated the fractional χ^2 difference, F_{crit} , equal to:

$$F_{\text{crit}} = \frac{(\chi_{PSF}^2 - \chi_{\text{Sérsic}}^2)}{\chi_{\text{Sérsic}}^2}, \quad (3)$$

where χ^2 is measured from the two model fits (Bond et al. 2009). Ryan et al. (2012) determined that for ERS ETGs observed in F160W, $F_{\text{crit}} \simeq 0.01$ can generally distinguish point-sources from well-resolved galaxies. Thirteen galaxies were measured to have $F_{\text{crit}} < 0.01$ and are designated “*Failed F_{crit}* ” in Table 1. Nine of these ETGs were originally noted for their compact morphology in Rutkowski et al. 2012, and a visual inspection of publicly available spectra¹⁵ confirmed that $\sim 50\%$ (7/13) of those ETGs were identified with [O II]3727 Å, or an unknown emission line, in their spectrum, potentially indicating the presence of a central star cluster or weak AGN. If the stellar light-profiles of these ETGs were relatively faint in comparison to a bright, spatially unresolved point source, this could explain the poor Sérsic profile fit. We exclude these galaxies from the subsequent analysis. At this stage, we also exclude one additional ETG because the light-profile of this galaxy was inextricably blended with a nearby galaxy and no accurate mask model could be determined. This ETG is indicated “*Not Fit*” in Table 1.

Next, we inspected the residual images produced by GALFIT by differencing the best-fit Sérsic model light-profile and the original input image. We found that $\sim 20\%$ ETGs that were not excluded by the above criteria were still poorly fit by a single Sérsic profile.¹⁶ These images typically showed an irregular, patchy, or “ring”-like structure (a bright core, bounded by an oversubtracted region) in their residual map. This structure may

¹⁴ Available publicly for download at http://dls.physics.ucdavis.edu/~rer/iGalFit/igalfit_v1.0/www/home.html.

¹⁵ Available online at http://archive.eso.org/archive/adp/GOODS/FORS2_spectroscopy_v3.0/index.html.

¹⁶ If GALFIT cannot converge on a parameter solution after a finite number of iterations, it will designate the poorly constrained parameter with an asterisk, “*.” The reduced χ^2 for the model fit may be small ($\lesssim 1$), but this solution should not be considered robust.

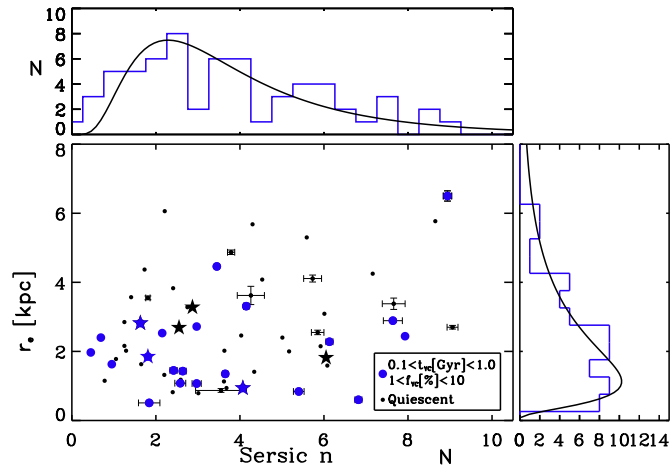


Figure 4. In Section 4.1, we measured the best-fit Sérsic function with index n , effective radius r_e , and ellipticity for the F160W light-profile of each ETG; here, Sérsic n is plotted against r_e for ETGs well-fit ($\chi^2 < 2$) in this analysis. Color of data points distinguish those ETGs identified with recent star formation from quiescent ETGs, well-fit ($\chi^2 < 2$; $N = 73$ ETGs—20 with RSF & 53 quiescent, respectively) in the morphological analysis. For clarity, we only overplot measurement uncertainties larger than 1%. ETGs identified with an AGN are designated with a filled star, with a color indicating the best-fit model. We fit a log-normal function to the distribution Sérsic index of half-light radii and plot these in the top- and right-hand panels. The best-fit mean Sérsic index and half-light radii, $\langle n \rangle = 2.1$ and $\langle r_e \rangle = 1.4$.

(A color version of this figure is available in the online journal.)

indicate the presence of an additional component, either in the core (a “cuspy” core or centrally concentrated star-forming region, see, e.g., Suh et al. 2010) or wings (possibly indicating an extended core stellar-disk component).

To improve our Sérsic model fit, we re-measured the light-profiles using a two-component model composed of a combined Sérsic model and the empirically defined PSF. We repeated our fitting of the light profiles with this model, measuring the best-fit model (M) that satisfied the criteria that (1) GALFIT parameter solution converged for each model, and (2) $M = \min\{\chi^2_{\text{Sérsic}}, \chi^2_{\text{Sérsic+PSF}}\}$, where the χ^2 was reported by GALFIT. In Table 1, ETGs whose light profiles were better modeled with this two-component spatial model are designated with χ^2_v in a boldface font. No solution could be found for two ETGs with either the one- (Sérsic only) or two- (Sérsic + empirical PSF) component model. Rather than attempt a fit with additional components, we designate the row value for these ETGs as “Fail to Converge” in Table 1, and do not consider these ETGs in the following discussion. In summary, 86 of 102 ETGs were well-fit ($\langle \chi^2_v \rangle = 0.54$) with either the one- or two-component Sérsic model.

In Figure 4, we plot the best-fit half-light radii (converted to a physical scale of kiloparsecs, assuming the spectroscopic distance) against the measured Sérsic index, with the symbol colors indicating the age of the young stellar population, t_{GC} . The mean Sérsic index ($\langle n \rangle$) equals 3.7 ± 2.1 and the mean half-light radius of $\langle r_e \rangle$ equals 2.9 ± 1.88 kpc. In the top panel of Figure 4, we plot a log-normal function fit to the distribution of n , where $\langle n \rangle = 2.1$, $\sigma = 1.2$ and skewness, γ , equals 1.6. In the right panel of Figure 4, we plot a log-normal function fit to the distribution of r_e , with a best-fit mean, variance (in kpc), and skewness equal to 1.4, 1.3, and 2.0, respectively. In general, there is no strong correlation observed between characteristics of the young stellar populations identified from the analysis of Section 3 and the morphology of these ETGs, i.e., recent star formation is

observed for ETGs with both disk ($n < 2.5$) and bulge-like ($n > 2.5$) morphologies. We note that the mean Sérsic index for high-mass ETGs ($M > 10^{10.5} M_\odot$) equals $\langle n \rangle = 4.2$ ($\sigma = 2.2$); the mean index measured for low-mass ETGs equals $\langle n \rangle = 2.2$ ($\sigma = 1.2$). For a discussion of the possible implications of these results for the evolution of ETGs at intermediate redshift, we refer the reader to Section 5.

4.2. ETGs and Likely Companions

Mergers of companions with massive ETGs are implicated in theory and observation to explain the recent star formation observed in the latter. The space density of *major* ($\mu = (M_{\text{comp}}/M_{\text{ETG}}) \sim 1$, i.e., equal mass) mergers is not high enough to account for the observed star formation in intermediate to high-redshift ETGs (e.g., López-Sanjuan 2010, 2012; Kaviraj et al. 2013b). Minor ($\mu \geq 1:4$) mergers occur more frequently than major mergers, and as a result are a more viable mechanism for introducing gas into ETGs (Kaviraj et al. 2013a). Due to the relatively short destruction timescales of companions in minor mergers (Peirani et al. 2010), catching such mergers “in the act” in order to directly correlate recent mergers with the incidence of recent star formation is not feasible with this small sample. Instead, the presence of companion galaxies can be used as a proxy for future mergers, as the infall times are markedly longer ($\gg 1$ Gyr; Tal et al. 2013). In the following sections, we outline (Section 4.2.1) and apply (Section 4.2.2) a method for measuring the number of *likely* companions for each ETG.

4.2.1. Likely Companions to ETGs: Method

In simplest terms, we want to identify galaxies in close proximity to each ETG. To do this, we define a volume of interest, V , centered on each ETG with dimensions (on the plane of the sky) of $\{X, Y\} = \{X_{\text{ETG}} \pm 100 \text{ kpc}, Y_{\text{ETG}} \pm 100 \text{ kpc}\}$. The third spatial dimension is proportional to the relative velocity of a galaxy in this volume. Here we adopt $v_{\text{comp}} = v_{\text{spec,ETG}} \pm 750 \text{ km s}^{-1}$. The dimensions of this volume are comparable to the definition applied in studies of pairs of galaxies at similar redshifts (e.g., Ryan et al. 2008; López-Sanjuan et al. 2010). We specifically select this volume because the likelihood of a merger of the ETG and the companion(s) by $z \simeq 0$ is predicted to be greater than 50 from simulations (Tal et al. 2013).

Not all galaxies located in this search region are likely companions, though. If the three-dimensional spatial positions of the galaxies within this region are well-constrained by a spectroscopic redshift, then measuring the companion number to each ETG is a simple counting exercise and the number of likely companions equals exactly the number of galaxies in the search region. In practice, identifying likely companions is more difficult because neither high-resolution imaging *or* complete spectroscopic data are available for all possible companions to ETGs in the ERS field, despite extensive efforts. In Rutkowski et al. (2012) we estimated the spectroscopic redshift deficit for visually classifiable (i.e., early or late-type) galaxies in the ERS field, and the fraction *without* measured spectroscopic redshifts may be as large as $\sim 75\%$. This spectroscopic incompleteness arises from technical limitations. First, spectroscopic redshift campaigns are limited by the apparent brightness of the observed galaxies. The Vanzella et al. (2008) spectroscopic survey of this field, for example, is likely to be only $\sim 10\%$ – 20% complete for the faintest galaxies ($F850LP > 25 \text{ mag}$) including ETGs. Note that this spectroscopic incompleteness also implies a mass incompleteness for the catalog of potential companions. Second,

quiescent ETGs, which lack significant line-emission, may be undetected because the Ca 4000 Å broad absorption complex cannot be bracketed from the ground at the high redshift range for this sample. Third, the ground-based spectroscopic candidate selection is typically done in the i band ($i \lesssim 22\text{--}24$ mag), but for the reddest $z \gtrsim 1$ ETGs, our H -band selection selects additional candidates for which spectroscopic redshift cannot be well constrained due to the atmosphere.

We measured photometry in all ten *HST* ACS and WFC3 filters for all galaxies in stamps, centered on the ETG, with an area equal to $\pi \times (100 \text{ kpc})^2$ (equivalently, stamp sizes with widths of 250–500 pixels at $0.35 \lesssim z \lesssim 1.5$) using *SExtractor* in dual-image mode. The F160W image was used as the detection image, and we applied the *SExtractor* detection criteria outlined in Rutkowski et al. (2012). After excluding objects that were located on or near the edges of the search region, we fit the observed photometry in all filters using the EAZY (Brammer et al. 2008) software to measure the galaxies’ photometric redshifts. The SEDs were fit with all the combinations of the SED templates¹⁷ provided with EAZY. We refer the readers to the EAZY manual¹⁸ for full details regarding this spectral template library, but note that these models generally represent the range of SFHs for galaxies at intermediate redshifts. We then produced a list of *possible* companions within a broad redshift range ($z_{\text{ETG}} \pm 0.25$) for each ETG. We matched the photometric redshift catalogs of all galaxies with existing spectroscopic redshift catalogs for the GOODS-S field from the literature, where available, to produce a catalog of *possible* companions for each ETG. Possible companions that were identified in both catalogs were assigned the higher-precision spectroscopic redshift. Few companions in each stamp were measured with spectroscopic redshifts ($N < 3$, at most).

We further reduced the catalog of possible companions by applying a magnitude selection, requiring the F160W magnitude measured for the possible companion to meet the criterion $m_{\text{F160W,comp}} < m_{\text{F160W,ETG}} + 2.5$. If the stellar mass-to-light ratios of these galaxies are similar, this implies that the stellar mass ratio of the pairs are $1 \lesssim \mu \lesssim 10$.

We apply a probability method for measuring N_c , the number of likely companions, motivated by the formalism defined first in López-Sanjuan et al. (2010). This method formally incorporates the measurement uncertainty in the photometric redshift of a galaxy into the measurement of N_c . This is accomplished by assuming that the likelihood of identifying a galaxy in the volume of interest as a companion to the ETG is proportional to the quality of the redshift. Specifically, if a galaxy has a spectroscopic redshift, the redshift probability function (or more generally, the “PF”) defining the likely position of a galaxy with respect to the volume of interest, is the Dirac delta function, which is equal to one within the volume and zero elsewhere. If a galaxy has a photometric redshift, López-Sanjuan et al. assume that its PF is Gaussian. The EAZY software reports a unique redshift PF for each galaxy, which we adopt instead for possible companions that do not have spectroscopic redshifts. To measure the number of likely companions, we (1) integrate the probability of each system of galaxies—in each integration, one member is always fixed to be the ETG—to be a pair, and (2) weight by the sum of the probabilities that each galaxy exists in the volume of interest to measure the weighted pair probability. We then sum over all weighted pair probabilities for all possible

pairs to define N_c . For complete details on this method, we refer the reader to the [Appendix](#).

4.2.2. Likely Companions to ETGs: Results

Applying the López-Sanjuan formalism we find that the total number of likely companions (N_c , defined as the sum of the individual system contributions, ν_k , as outlined in the [Appendix](#)) is only greater than one if the galaxies within the volume of interest are measured with a *spectroscopic* redshift. Conversely, *no* ETGs were measured with $N_c \gtrsim 1$ if *all* possible companions had *only* measured photometric redshifts. For systems—with possible companions measured only with photometric redshifts—to contribute $\nu_k \simeq 1$, the uncertainty in the companions’ redshift must be quite small. Only in the idealized case where the photometric redshift of the possible companion equals the spectroscopic redshift of the ETG, will a Gaussian PF with $\sigma_z \lesssim 10^{-3}$ (or, equivalently an uncertainty in velocity equal to $\sigma_v \lesssim 10^2 \text{ km s}^{-1}$) contribute $N_c^j \sim 1$. No possible companions with photometric redshifts and such narrow PFs met the selection criteria (Section 4.2.1). In practice, the PFs associated with photometric redshifts for possible companions were measured with $\sigma_z \simeq 10^{-1}$. Uncertainties of this magnitude imply contributions to the total number of likely companions in these pairs of $\lesssim 10^{-2}$. The total number of galaxies with only photometric redshifts (i.e., no companions considered had *spectroscopic* redshifts) was never greater than seven in the search region. Thus, the cumulative contribution of these system was never greater than $N_c \simeq 0.1$. Increasing the search volume could increase the number of possible companions considered. Doing so will also decrease the likelihood for a merger by $z \sim 0$ below $\sim 50\%$ based on the results of Tal et al. 2013. We cannot expect that the PFs of the possible companions will be appreciably improved by the use of more broad or medium band filters. In the zCOSMOS survey, for example, Knobel et al. (2012) used imaging in 30 medium- and broadband filters to measure photometric redshifts, and found even this extensive coverage to be insufficient for identifying individual pairs and groups for galaxies at $z \lesssim 1$.

We have measured more than one likely companion for $\sim 20\%$ (16/102) of the ETGs where the companions’ redshifts were spectroscopically confirmed. As such, this measurement is a strong *lower* limit on the frequency of companions to ETGs. In Table 2, we present a list of these ETGs. We include 1σ uncertainties associated with N_c , measured with an empirical jackknife technique following Efron (1982), where:

$$\sigma^2 = (N - 1) \sum_{j=1}^N \frac{(N_c^j - N_c)^2}{N}, \quad (4)$$

here N_c^i is the total number of galaxies excluding the contribution from the i th system, N_c is the total number of likely companions, N equals the total number of galaxies, and the sum is measured over the set of j possible companions. In Table 2, we also include the number of possible companions with photometric (Column 3) and spectroscopic (Column 4) redshifts that contributed to the measurement of N_c .

We measure the average characteristics for galaxies with and without companions for the subset of ETGs ($N = 33$) measured with recent star formation ($1 < f_{\text{YC}}[\%] < 10$; $0.1 < t_{\text{YC}}[\text{Gyr}] < 1$) in Section 3.2 and with morphological parameters that were well fit ($\chi_v^2 < 2$). For ETGs with $N_c < 1$ ($N = 26$), the mean Sérsic index, mass, and sizes equal $\langle n, M[M_\odot], r_e[\text{kpc}] \rangle \simeq (3.6 \pm 2.5, 10.5 \pm 0.59, 2.6 \pm 1.7)$,

¹⁷ These spectral templates are derived from the PÈGASE model SEDs (Fioc & Rocca-Volmerange 1997) by the authors of the EAZY software.

¹⁸ Available online at http://www.astro.yale.edu/eazy/eazy_manual.pdf.

Table 2
Number of Likely Companions

GOODS ID	N_c	n_{spec}	n_{phot}
J033205.09-274514.0	3.03 ± 1.64	7	3
J033206.27-274536.7	1.01 ± 0.82	2	1
J033207.55-274356.6	1.02 ± 0.90	4	1
J033208.53-274217.7	1.01 ± 0.87	3	1
J033210.04-274333.1	1.01 ± 0.77	3	1
J033210.12-274333.3	1.02 ± 0.91	5	1
J033211.21-274533.4	1.01 ± 0.87	3	1
J033211.61-274554.1	1.01 ± 0.82	2	1
J033212.20-274530.1	1.01 ± 0.82	2	1
J033212.31-274527.4	1.02 ± 0.87	3	1
J033214.45-274456.6	1.01 ± 0.89	4	1
J033219.02-274242.7	1.01 ± 0.87	3	1
J033226.71-274340.2	1.01 ± 0.93	6	1
J033231.84-274329.4	1.02 ± 0.90	4	1
J033233.40-274138.9	2.01 ± 1.22	2	2
J033235.10-274410.7	1.00 ± 0.82	2	1

Notes. Column 2: number of likely companions, with 1σ uncertainties measured from an empirical jackknife technique (Section 4.2.2). Columns 3 and 4: number of photometric and spectroscopic possible companions.

with 1σ dispersion reported on each mean value. The mean age and mass fraction of young stars for this subset equals $\langle t_{YC}[\text{Myr}], f_{YC}[\%] \rangle \simeq (325 \pm 185, 3 \pm 2)$. For the subsample of ETGs with $N_c \geq 1$ ($N = 6$), $\langle n, M[M_\odot], r_e[\text{kpc}] \rangle \simeq (3.9 \pm 1.5, 10.7 \pm 0.52, 2.3 \pm 1.9)$. The mean age and mass fraction of young stars for this subset equals $\langle t_{YC}[\text{Myr}], f_{YC}[\%] \rangle \simeq (260 \pm 130, 2 \pm 1.9)$. If these data are normally distributed in each sample, a two-sample t -test shows that the mean parameters presented for ETGs with, and without, companions are not statistically significant. Whether these measurements are in fact normally distributed is difficult to determine given the small sample sizes, but we conclude that the measured properties of ETGs with and without companions are indistinguishable.

5. THE SIZE–MASS RELATION FOR INTERMEDIATE REDSHIFT ETGS

It is useful to frame the results from our analysis in the context of the physical size and stellar mass (i.e., size–mass) relationship of galaxies, a touchstone for both theoretical and observational studies of ETG evolution. In the following sections, we present this measured bivariate distribution for our intermediate redshift ETGs (Section 5.1). We discuss the measured distributions in the context of previously published size–mass relationships and the implications for the evolution of intermediate redshift ETGs in Section 5.2.

5.1. The Observed Size–Mass Relation

In Figure 5, we plot the half-light radii of the ETGs (Section 4.1) against the stellar masses derived from the optical–IR SED fits (Section 3.1). Here, we only plot ETGs that were well-fit ($\chi^2_\nu < 2$) in the analyses of *all* sections. For reference, we plot the mean uncertainties in half-light radius and stellar mass for an ETG with an average size and mass. We overplot three empirical size–mass relationships observed for local ETGs and late-type galaxies (dotted and solid black curves, respectively; reproduced from Shen et al. 2003) and intermediate redshift ($1.0 < z < 1.5$) ETGs (dashed line; from Williams et al. 2010)—these relationships are *not* fits to the data. We indicate ETGs with likely ($N_c \gtrsim 1$) companions within $\Delta v = 750 \text{ km s}^{-1}$

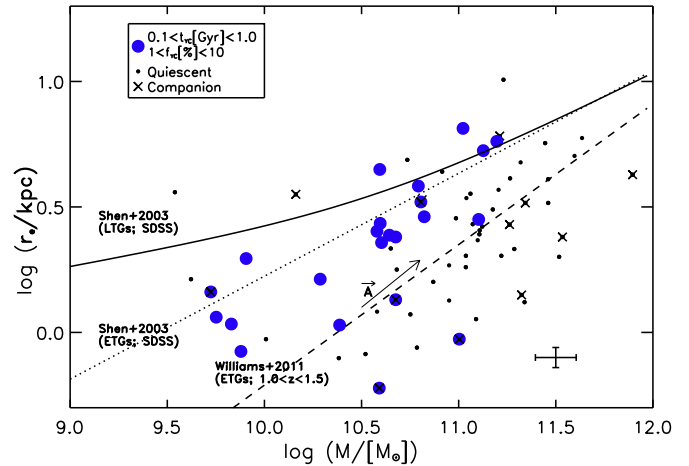


Figure 5. We summarize the results of the SED modeling, morphological, and companion analyses here, plotting the size and stellar mass for all ETGs that were well-fit (i.e., $\chi^2_\nu < 2$) in both the SED modeling (Section 3) and morphological (Section 4) analyses ($N = 73$). The representative mean uncertainty in the size and mass are provided in the bottom right. Quiescent ETGs identified from the SED fitting are plotted as small, black points; ETGs with likely companions (Section 4) are indicated by a black “x.” Note that only those galaxies with spectroscopically confirmed redshifts are measured to be likely companions to the ETGs, using the statistical method outlined in Section 4.2.1. ETGs identified in the Section 3.2 analysis with evidence of recent star formation ($f_{YC} < 10\%$; $t < 1$ Gyr) are indicated with blue, filled circles. For reference, we overplot an empirical intermediate-redshift size–mass relationship for ETGs (dashed; Williams et al. 2010). We overplot the Shen et al. (2003) low-redshift size–mass relationships measured for early-type (dotted) and late-type (solid) galaxies. Note, massive ($M > 10^{10.5} M_\odot$) ETGs with recent star formation appear to be loosely clustered near the Shen et al. low-redshift ETG size–mass relationship, whereas quiescent ETGs, particularly those with companions, appear to have smaller average sizes and cluster toward the high-redshift relationship of Williams et al. (2010). We overplot a preferred vector (\vec{A}), indicated by the thin-line arrow originating at $\log(M, r_e) \simeq (10.5, 0.1)$, which appears to bisect those ETGs with RSF and those with $N_c > 1$. We use the perpendicular distance of these data measured with respect to this vector in Section 5.2 to test whether this apparent clustering is statistically significant.

(A color version of this figure is available in the online journal.)

with an “x” symbol. ETGs that were best-fit (Section 3.2) with a minor component of young ($1\% < f_{YC}[\%] < 10\%$ and $0.1 < t[\text{Gyr}] < 1$) stars are plotted as filled points with a color defined by the key in the figure. ETGs not meeting these additional criteria are plotted as small, filled circles.

A few trends appear in Figure 5 that may provide some insight into the mechanism(s) inducing RSF in intermediate redshift ETGs. First, there does not appear to be a mass dependency in the distribution of ETGs that have experienced recent star formation ($t < 1$ Gyr). Although many of the low-mass galaxies ($M < 10^{10.5}$) are likely to have experienced a minor burst of RSF in the previous ~ 1 Gyr, RSF is also observed in high-mass ETGs. Second, we note that high-mass ($M > 10^{10.5} M_\odot$) ETGs with RSF and those (albeit few) ETGs with likely companions ($N_c \geq 1$) appear to occupy unique sectors in the size–mass parameter space. Recently, star-forming ETGs appear to be distributed on or near the Shen et al. (2003) low-redshift size–mass relation. In contrast, quiescent ETGs—in particular, ETGs with companions—appear on or near the intermediate-redshift size–mass relationship for ETGs. The tight apparent clusters, at $M \simeq 10.5$ and $11 M_\odot$, within the broader mass–size distributions are populated by ETGs over a wide redshift range ($0.6 < z < 1.4$), although we reiterate the important note from Section 3.2 that these ERS data are most sensitive to recent star formation at the lower ($z \lesssim 1$) redshift range of our samples.

We confirm with a two-sample t -test that the means of each of these distributions are distinguishable (i.e., the null hypothesis is rejected at $\gtrsim 95\%$, if the data are normally distributed). To better illustrate this apparent clustering, we collapse the bivariate size–mass distributions of these two populations of ETGs along a preferred vector that is approximately parallel to the empirical size–mass relationships for high-mass ETGs (Williams et al. 2010). This vector—a *non-unique* bisection that was estimated from a visual inspection of the distributions of these two populations—is overplotted (indicated \vec{A} in Figure 5) for reference in Figure 5 as a thin-line arrow originating at $\log(M, r_e) \simeq 10.5, 0.1$. For each of the ETGs with RSF and with likely companions we measure the magnitude of the perpendicular distance, $d\vec{A}$ from the preferred vector \vec{A} . A histogram of these distances is plotted in black ($N_c \geq 1$) and red (RSF), respectively, in Figure 6. Additionally in Figure 6, the best-fit Gaussian function to each distribution is overlotted in the same color. Here, the mean for all quiescent high-mass ETGs is distinguishable (null hypothesis is rejected at $>99.5\%$ level) from ETGs with recent star formation, with the median distinguished at 5σ . If the ETGs with RSF (ETGs with $N_c \geq 1$) that lie above (below) the vector \vec{A} are removed for the purposes of refining the fit of the Gaussian to each distribution, the means of the two distributions can be distinguished at 7σ .

5.2. Implications for the Evolution of ETGs from Their Size–Mass Distribution

The observed diversity in the colors and SFHs of our ETGs is difficult to reconcile with models that would predict more uniformly passive characteristics for such galaxies. For example, Peng et al. (2010) presented a model in which massive ($M \gtrsim 10^{10} M_\odot$) galaxies reside in a “mass-quenching” regime, in which these galaxies’ evolution is dominated by internal feedback, in contrast to environmental factors. This model predicts that 65%–80% of massive ETGs in our sample will reside on the red sequence. We do not observe such a mass-dependency for star formation in our sample.

The lack of a strong mass-dependent trend of observed RSF may be interpreted as support for star formation in ETGs as a *stochastic* process (e.g., RSF is related to the environment). Although the number of ETGs with companions is small ($N = 10$), the distinction in the distributions may still be instructive of the process(es) driving recent star formation or transforming the sizes of massive ETGs. We note that the companion galaxies to the $\sim 20\%$ of ETGs identified with companions (Section 4.2.2) are bright ($m_{F606W} \lesssim 23$ mag) and therefore massive,¹⁹ and have blue UV–optical rest-frame colors ($\langle (NUV - V)_r \rangle \simeq 2.5$ mag). This suggests that these companions are relatively gas-rich. From simulations, these companions will likely merge ($\gtrsim 50\%$) by $z \sim 0$ (Tal et al. 2013). If these companions do not consume their cold-gas reserves in advance of a future merger, then some degree of new star formation should be expected in the ETGs.

Alternatively, the measured size–mass distribution and the observed characteristics of ETGs with RSF could be interpreted as evidence for a progenitor bias. In effect, in our sample we may have caught recently quenched galaxies “in the act” as they transitioned toward the red sequence. For a comparison with high ($z \sim 1.5$) redshift studies, consider the recent results

¹⁹ This is a systematic effect, as brighter galaxies are more likely to have spectroscopically confirmed redshifts and thus have been identified by the analysis in Section 4.2.2, which limits the range of mass ratios we consider to $\mu \gtrsim 1.2$.

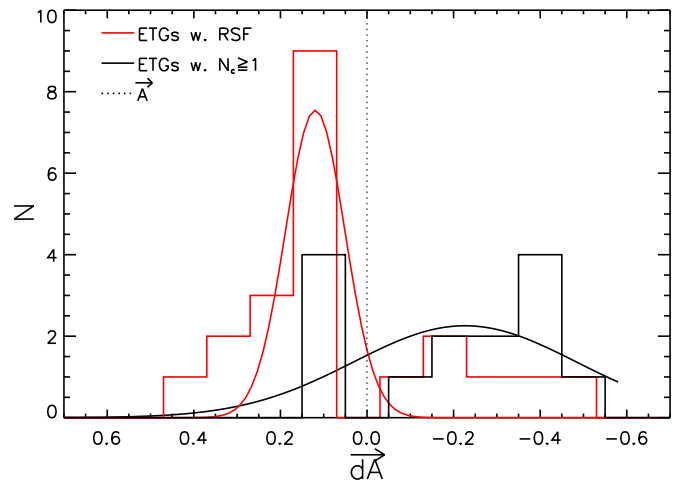


Figure 6. In Section 5.1, we noted that high-mass ($M \gtrsim 10.5 M_\odot$) ETGs with recent star formation appear to be distributed near the low-redshift ($z \sim 0$) empirical size–mass relationship. In contrast, quiescent ETGs and particularly ETGs with $N_c \geq 1$ cluster, although with larger dispersion, near the intermediate redshift ($1.0 < z < 1.5$) empirical size–mass relationship. Here, we plot histograms of these populations’ perpendicular distances, $d\vec{A}$, from the preferred vector, \vec{A} (see Figure 5) for ETGs with $N_c \geq 1$ (black) and RSF (red), respectively, with Gaussian fits to each distribution overlotted. In Section 5.2, we find that these means of each distribution are distinguishable by a two-sample t -test (i.e., the null hypothesis is rejected at $\gtrsim 95\%$). We discuss the implications of this distinction in Section 5.2, with respect to the mechanism for inducing RSF in intermediate-redshift ETGs.

(A color version of this figure is available in the online journal.)

of Bedregal et al. (2013, hereafter “B13”), which selected ~ 40 passive galaxies from the *HST* WFC3 IR grism pure-parallel WISP survey (PI: M. Malkan). Differences in the selection of galaxies between the B13 sample and our own makes a direct comparison difficult—B13 used rest-frame optical color and mass to select relatively more massive ($\langle M \rangle \simeq 10^{11} M_\odot$) passive galaxies for study, whereas our selection is primarily morphological and does not by design *preclude* minor recent star formation—but the B13 results are germane to this discussion. First, B13 also observe a diversity in the average ages of the stellar populations in massive, quenched galaxies, with approximately 30% of the galaxies residing off the passive, red sequence. They interpret the homogeneous spread in the mass of the quenched galaxies on and off of the red-sequence as evidence that multiple mechanisms are responsible for the quenching of star formation in high mass galaxies, and the authors emphasize that the spectra of these galaxies imply that they are transitioning from a former period of intense star formation at high ($z \gg 2$) redshift. B13 also predict that the massive galaxies in their sample would join the red sequence by $z \sim 1$, implying that young stellar populations in quenched intermediate redshift ETGs could still be directly detectable in our broadband UV data.

Furthermore, at low-redshift ($z \lesssim 0.1$), Wyder et al. (2007) have suggested that a continuum of young and old transitioning galaxies populate the UV–optical low-redshift ($z \lesssim 0.1$) green valley. In our sample, among massive ($> 10^{10.5} M_\odot$) recently star-forming ETGs we do find disk-like ($n < 2.5$) ETGs, which supports an interpretation that the observed RSF could be associated with the quenching of star formation in higher redshift progenitors of local ETGs. We note, however, that the mean Sérsic index measured for these high-mass ETGs (see Section 4.1) is large ($\langle n \rangle \simeq 4.2$), and is similarly large for both the sample of recently star-forming and quiescent high-mass

ETGs ($\langle n \rangle \simeq 4.5$). It is important to note that the high mean Sérsic does not necessarily imply that the histories of massive galaxies have followed a relatively quiescent evolution. Carollo et al. (2013), in the study of thousands of $z \sim 1$ ETGs, found that $\sim 90\%$ of high mass ($M > 10^{10.5} M_{\odot}$) star-forming disk galaxies are bulge-dominated in their light-profiles.

We observe (1) the association of companions with ETGs, albeit a small fraction of the total number of ETGs in the catalog; (2) the presence of bulge-dominated profiles in both compact, quiescent, and recently star-forming ETGs; (3) recent star formation independent of ETG stellar masses; and (4) a distinction between the size–mass distributions of ETGs with RSF and ETGs with likely companions. Considered jointly, these observations imply that both the introduction of quenched galaxies and mergers both likely play a non-negligible role in the formation of young stars and size-mass evolution of intermediate redshift ETGs.

This conclusion is most severely limited by the relatively small number of ETGs identified with possible companions that have *spectroscopic* redshifts. We have obtained spectroscopic observations of an additional ~ 100 intermediate redshift ETGs and possible companions in the COSMOS field with MMT Hectospec in order to expand the sample size of ETGs and their possible companions at $0.35 \lesssim z \lesssim 1.5$. This survey program specifically targeted both previously unobserved bright ($F160W < 21$ mag) ETGs, as well as their bright companions. Repeating the companion analysis presented in Section 4 with the increased spectroscopic redshift statistics—combined with deep *U*-band observations (< 27.5 mag) we obtained at the Large Binocular Telescope—will improve the observational constraints of the role of relatively gas-rich minor mergers in the mass-size evolution and stellar mass-assembly of ETGs.

6. CONCLUSION

We used *HST* WFC3 panchromatic data to study the mechanism(s) that induce the observed recent star formation, here confirmed in *at least* 40% of the intermediate redshift ($0.35 \lesssim z \lesssim 1.5$) ETGs. This measurement is bounded by similar measurements of the fraction of ETGs with RSF observed at high (60%; e.g., Kaviraj et al. 2013a) and low (30%; e.g., Kaviraj et al. 2007) redshift. Together, these measurements suggest that the frequency of RSF in ETGs generally declines with decreasing redshift. We caution a strict interpretation of this result, noting that each of these measurements is limited by the photometric completeness (particularly at UV wavelengths) of the surveys from which the fraction of RSF is observed. We cannot rule out a constant fraction of ETGs with RSF with respect to decreasing redshift from $z \sim 1.5$ to the local universe.

We find evidence for RSF in ETGs best-fit by disk- ($n < 2.5$) and bulge-like ($n > 2.5$) Sérsic profiles, with the mean Sérsic index increasing only weakly with mass. Furthermore, the prevalence of RSF in ETGs does not correlate with the mass of the galaxy. This result is at odds with a pure “mass-quenching” model of massive galaxy evolution (see Peng et al. 2010), which has been postulated for the low-redshift ($z < 0.1$) evolution of galaxies.

In addition, we find that massive ($M > 10^{10.5} M_{\odot}$) ETGs with evidence of RSF appear to be large on average and cluster toward the low-redshift size–mass relationship for ETGs measured by Shen et al. (2003). Quiescent, massive ETGs have smaller sizes, but with a larger dispersion than is measured for ETGs with RSF. This result suggests that the introduction of recently quenched star-forming galaxies into the green valley

and the red-sequence, may motivate the observed RSF and size–mass evolution observed since $z \sim 2$ (Carollo et al. 2013). We cannot rule out—due to the relatively small number of likely companions with confirmed spectroscopic redshifts—an environmental, gas-rich minor merger scenario that induces RSF in intermediate redshift ETGs. Considering the frequency of companions to ETGs with RSF, a large dispersion in the size-mass distributions and the presence of bulge- and disk-like light-profiles measured for quiescent and recently star-forming ETGs, we suggest that both the transition of disk-like progenitors to the red sequence *and* minor-merger/recent interactions are both important in the evolution of intermediate redshift ETGs. Future deep, large volume UV-optical surveys, in combination with deeper spectroscopic surveys that precisely measure the redshifts of the faint potential companions, will be ideally suited to differentiate the relative roles of environmental (e.g., minor mergers) and progenitor bias in motivating the observed frequency of RSF in intermediate redshift ETGs.

We note that the confirmation of recent star formation in ETGs at this redshift range required a significant investment in space-based, rest-frame UV-optical observations. We urge the community in future surveys of the star formation histories of massive galaxies at intermediate redshift to include deep UV rest-frame observations prior to the decommission of the *HST* in the coming decade.

This paper is based on Early Release Science observations made by the WFC3 Scientific Oversight Committee. We are grateful to the Director of the Space Telescope Science Institute, Dr. Matt Mountain, for generously awarding Director’s Discretionary time for this program. Finally, we are deeply indebted to the crew of STS-125 for refurbishing and repairing HST. Support for program #11359 was provided by NASA through a grant from the STScI, which is operated by the Association of Universities for Research Inc., under NASA contract NAS 5-26555. M.R. acknowledges support from a US State Department Fulbright Junior Research Fellowship in conjunction with the S. Korean government and Yonsei University. H.J. acknowledges support from the Basic Science Research Program through the National Research Foundation of Korea (NRF), funded by the Ministry of Education (NRF-2013R1A6A3A04064993). S.K.Y. was supported by the National Research Foundation of Korea (Doyak 2014003730). We thank C. Lopez-Sanjuan for helpful discussions and the anonymous referee for extensive comments that have improved this publication.

APPENDIX

COMPANION PROBABILITY

Numerous techniques exist for counting pairs and groups of galaxies for which photometric and/or spectroscopic redshifts have been measured. The distinctions between these methods arises from the treatment of the uncertainties ($\Delta z/(1+z) = 5\%–10\%$) in the three-dimensional positions of the galaxies. If the positions of galaxies are precisely measured in high-spatial-resolution images, then, for a set of galaxies with spectroscopically confirmed redshifts, the determination of the number of companions to any individual galaxy is simply a counting exercise. In deep broadband multi-wavelength surveys, the positions of the majority of galaxies are typically constrained only by photometric redshifts from broadband SED fitting. When the uncertainties on these redshifts are small, these measurements may still prove very useful in measuring

statistical trends for large samples of galaxies (e.g., the measurement of the pair fraction of galaxies or the merger rate) by incorporating the positional uncertainty as a weight in calculating the likelihood of whether two galaxies are companions.

López-Sanjuan et al. (2010) presented a statistical study of the pair fraction of galaxies at intermediate redshift, defining the number of pairs distributed among k systems at a redshift z_1 as:

$$\nu_k(z_1) = C_k P_1(z_1|\eta_1) \int_{z_m^-}^{z_m^+} P_2(z_2|\eta_2) dz_2 \quad (\text{A1})$$

where C_k is a constant normalizing the number of pair systems to unity, $P(z|\eta)$ the probability function (or, simply the PF referenced first in Section 4.2.1), and $[z_m^-, z_m^+]$ is the redshift range of interest. To measure ν_k , we define each of these terms as follows. The redshift range $[z_m^-, z_m^+]$ is defined for some range over which pairs are cosmologically meaningful; functionally, this equals $\{z_m^-, z_m^+\} = \{z_{\text{ETG}} \times (1 - \Delta v/c) - \Delta v/c, z_{\text{ETG}} \times (1 + \Delta v/c) + \Delta v/c\}$. We assume $\Delta v = 750 \text{ km s}^{-1}$, a range motivated by Tal et al. (2014) to include close pairs that will merge with a probability greater than 50% by $z \sim 0$. Incorporating the spatial positions of the possible companions, we can define the volume of interest, $V = \{X, Y, Z\}$, proportional to $\{X_{\text{ETG}} \pm 100 \text{ kpc}, Y_{\text{ETG}} \pm 100 \text{ kpc}, v_{\text{comp}} = v_{\text{spec,ETG}} \pm 750 \text{ km s}^{-1}\}$. In practice, López-Sanjuan define the probability function, $P(z|\eta)$, of identifying a galaxy in the redshift range with respect to the quality of its measured redshift. If a galaxy is measured with a spectroscopic redshift z_s , the probability of finding it within the range $\{z_m^-, z_m^+\}$ is given as $P_s(z|\eta) = \delta(z - z_s)$, where, δ is the Dirac delta function. If a galaxy in proximity to the volume of interest has a measured photometric redshift, z_p , its probability is defined as $P_p(z|\eta) = (1/\sqrt{2\pi}\sigma_{z_p}) \exp\{-(z_{\text{ETG}} - z_p)^2/2\sigma_{z_p}^2\}$. We use the EAZY photometric redshift software to calculate redshifts for galaxies within 100kpc of each ETG, and thus $P(z|\eta)$ equals the PF reported by EAZY for the best-fit model fit for each galaxy. Finally, C_k is functionally equivalent to $N_p^k = \int_{z_m^-}^{z_m^+} P_1(z_1|\eta) dz_1 + \int_{z_m^-}^{z_m^+} P_2(z_2|\eta) dz_2$. Summing $\nu(z)$ over all k -systems in all redshift intervals of interests yields the total number of likely companions (i.e., $N_c = \sum_k \nu_k(z_1)$). In Section 4.2.2 we apply this methodology for calculating likely companions to the ETGs within the volume of interest, fixing the redshift range ($[z_m^-, z_m^+]$) constant for all k pair systems potentially associated with each ETG.

As discussed in Section 4.2.2, we found that only those systems in which the possible companion galaxies were measured with spectroscopic redshifts were measured to have $N_c > 1$. This does not imply that the ETGs that had possible companions with only measured photometric redshifts had no likely companions. Instead, this stems directly from the PF curves associated with these photometric redshifts being too poorly constrained, implying that their contribution to N_c was never greater than ~ 0.05 , or similarly the probability of finding a galaxy in the volume of interest was too small ($\ll 1\%$).

For reference, the specific calculation we made here, based on the López-Sanjuan formalism may be easily conceptualized in terms of the joint probabilities that *any* galaxies in the volume of interest will be identified as an ETG companion. From the probability of sets, the cumulative union of probabilities of N independent events can be written in the standard notation as:

$$P\left(\bigcup_{i=1}^N E_x\right) = \sum_{1 \leq i_1 \leq i_2 \leq \dots \leq i_N \leq N} P(E_{i_1} \cap E_{i_2} \dots \cap E_{i_N}). \quad (\text{A2})$$

As an example, when $N = 3$, then $P(\bigcup_{i=1}^3 E_i)$ measured for three *independent* events E_A or E_B or E_C is

$$\begin{aligned} P(E_A \cup E_B \cup E_C) &= P(E_A) + P(E_B) + P(E_C) \\ &\quad - (P(E_A \cap E_B) + P(E_A \cap E_C) + P(E_B \cap E_C)) \\ &\quad + P(E_A \cap E_B \cap E_C). \end{aligned} \quad (\text{A3})$$

Here, an event E_i is defined as the likelihood of a galaxy in the volume of interest to be identified as a companion to an ETG. The limits on the union of probabilities are $0 \leq P(\bigcup_{i=1}^N E_x) \leq 1$. In the case of sets of galaxies that include small numbers of possible companions, each with poorly constrained (i.e., broad) PFs, $P(\bigcup E_i) \rightarrow 0$. Alternatively, in sets with small numbers of possible companions that have well-constrained PFs (the case for galaxies measured with spectroscopic redshifts) or sets that include *numerous* possible companions with poorly constrained PFs (potentially the case for groups of galaxies with well-constrained photometric redshifts) then $P(\bigcup E_i) \rightarrow 1$. Using a similar notation to López-Sanjuan et al., the probability that a galaxy is located in the volume of interest, V , can then be defined as $P(E_k) = P(z_{\text{ETG}}) \times \int_V (\text{PF})$, with the functional form of PF either the Dirac delta function (for galaxies with spectroscopic redshifts) or a Gaussian or other function as discussed previously for galaxies with photometric redshifts.

Of course, this method will not improve the probability that any individual ETG galaxy system will be considered a pair, as the PFs are fixed by the quality of the data. But, if a uniform brightness is applied in defining systems of possible companion systems (as we did in Section 4.2), Equation (A2) provides a more generalized extension of the López-Sanjuan formalism. When we apply the more general method to our data, the measurement of the number of likely companions is identical to the measurement of N_c measured using the López-Sanjuan formalism presented in Section 4.2.2. We again find that *no* ETGs are identified with likely companions using this alternative method, if the galaxies within the volume of interest are measured only with photometric redshifts. Only possible companion galaxies with spectroscopically confirmed redshifts are found to be likely companions to these catalog ETGs.

REFERENCES

- Barro, G., Faber, S. M., Prez-Gonzalez, P. G., et al. 2013, *ApJ*, **765**, 104
 Bedregal, A., Scarlata, C., Henry, A. L., et al. 2013, *ApJ*, **778**, 126 (B13)
 Bender, R., Burstein, D., & Faber, S. M. 1992, *ApJ*, **399**, 462
 Bertin, E., & Arnouts, S. 1996, *A&A*, **117**, 393
 Bond, N. A., Gawiser, E., Gronwall, C., et al. 2009, *ApJ*, **705**, 639
 Brammer, G. B., van Dokkum, P. G., & Coppi, P. 2008, *ApJ*, **686**, 1503
 Bruzual, A. G., & Charlot, S. 2003, *MNRAS*, **344**, 1000 (BC03)
 Calzetti, D., Armus, L., Bohlin, R. C., et al. 2000, *ApJ*, **533**, 682
 Carollo, M., Bschorr, T. J., Renzini, A., et al. 2013, *ApJ*, **773**, 112
 Cassata, P., Giavalisco, M., Guo, Y., et al. 2011, *ApJ*, **743**, 96
 Cassata, P., Giavalisco, M., Williams, C. C., et al. 2013, *ApJ*, **775**, 106
 Chiosi, C., & Carraro, G. 2002, *MNRAS*, **335**, 335
 Daddi, E., Renzini, A., Pirzkal, N., et al. 2005, *ApJ*, **626**, 680
 Damjanov, I., McCarthy, P. J., Abraham, R. G., et al. 2009, *ApJ*, **695**, 101
 Dekel, A., Sari, R., & Ceverino, D. 2009, *ApJ*, **703**, 785
 DeVaucouleurs, G. 1961, *ApJS*, **5**, 233
 de Zeeuw, P. T., Bureau, M., Emsellem, E., et al. 2002, *MNRAS*, **329**, 513
 Dickinson, M., Giavalisco, M., & the GOODS Team, 2003, in Proc. of the ESO and Universitäts-Sternwarte München Workshop, The Mass of Galaxies at Low and High Redshift, ed. R. Bender & A. Renzini (Verlag: Springer), 324
 Efron, B. 1982, *The Jackknife, the Bootstrap and Other Resampling Plans* (Philadelphia, PA: SIAM)
 Eliche-Moral, M. C., Prieto, M., Gallego, J., et al. 2010, *A&A*, **519**, A55
 Faber, S., Tremaine, S., Ajhar, E. A., et al. 2007, *ApJ*, **665**, 265
 Fan, L., Lapi, A., Bressan, A., et al. 2010, *ApJ*, **718**, 1460

- Fan, L., Lapi, A., De Zotti, G., & Danese, L. 2008, *ApJL*, **689**, L101
- Ferreras, I., & Silk, J. 2000, *ApJ*, **532**, 193
- Fioc, M., & Rocca-Volmerange, B. 1997, *A&A*, **326**, 950
- Fukugita, M., Hogan, C. J., & Peebles, P. J. E. 1998, *ApJ*, **503**, 518
- Giavalisco, M., Ferguson, H. C., Koekemoer, A. M., et al. 2004, *ApJL*, **600**, L93
- Han, Z., Podsiadlowski, P., & Lynas-Gray, A. E. 2007, *MNRAS*, **380**, 1098
- Hopkins, P., Bundy, K., Murray, N., et al. 2008, *MNRAS*, **398**, 898
- Hopkins, P., Cox, T. J., Dutta, S. N., et al. 2009, *ApJS*, **181**, 135
- Jeong, H., Bureau, M., Yi, S. K., et al. 2007, *MNRAS*, **376**, 1021
- Kannappan, G., Guie, J. M., & Baker, A. J. 2009, *AJ*, **138**, 579
- Kaviraj, S. 2014a, *MNRAS*, **437**, L41
- Kaviraj, S. 2014b, *MNRAS*, **440**, 2944
- Kaviraj, S., Cohen, S., Ellis, R. S., et al. 2013b, *MNRAS*, **428**, 925
- Kaviraj, S., Cohen, S., Windhorst, R. A., et al. 2013a, *MNRAS*, **429**, L40
- Kaviraj, S., Khochfar, S., Schawinski, K., et al. 2008, *MNRAS*, **388**, 67
- Kaviraj, S., Rey, S.-C., Rich, R. M., Yoon, S.-J., & Yi, S. K. 2007, *MNRAS*, **381**, L74
- Kaviraj, S., Tan, K.-M., Ellis, R. S., & Silk, J. 2011, *MNRAS*, **411**, 2148
- Kennicutt, R. 1998, *ARA&A*, **36**, 189
- Khochfar, S., & Burkert, A. 2003, *ApJL*, **597**, L117
- Knobel, C., Lilly, S. J., Iovino, A., et al. 2012, *ApJ*, **753**, 121
- Komatsu, E., Smith, K. M., Dunkley, J., et al. 2011, *ApJS*, **192**, 18
- Kormendy, J., Fisher, D. B., Cornell, M. E., & Bender, R. 2009, *ApJS*, **182**, 216
- Krajinovic, D., Alatalo, K., Blitz, L., et al. 2013, *MNRAS*, **432**, 1768
- Larson, R. B. 1974, *MNRAS*, **166**, 585
- López-Sanjuan, C., Balcells, M., Prez-Gonzalez, P. G., et al. 2010, *A&A*, **518**, A20
- López-Sanjuan, C., Le Fèvre, O., Ilbert, O., et al. 2012, *A&A*, **548**, A7
- Lucero, D. M., & Young, L. M. 2007, *AJ*, **134**, 2148
- Lucero, D. M., & Young, L. M. 2013, *AJ*, **145**, 56
- Matteucci, F. 1994, *A&A*, **288**, 57
- Morrissey, P., Schiminovich, D., Barlow, T. A., et al. 2005, *ApJS*, **619**, L7
- Mostek, N., Coil, A. L., Cooper, M., et al. 2013, *ApJ*, **767**, 89
- Naab, T., Johansson, P. H., & Ostriker, J. P. 2009, *ApJL*, **699**, L178
- Newman, A. B., Ellis, R. S., Bundy, K., & Treu, T. 2012, *ApJ*, **746**, 162
- O'Connell, R. W. 1999, *ARA&A*, **37**, 603
- Oke, J. B., & Gunn, J. E. 1983, *ApJ*, **266**, 713
- Papovich, C., Dickinson, M., & Ferguson, H. C. 2001, *ApJ*, **559**, 620
- Peirani, S., Crockett, R. M., Geen, S., et al. 2010, *MNRAS*, **405**, 2327
- Peng, C., Ho, L. C., Impy, C. D., & Rix, H.-W. 2002, *AJ*, **124**, 266
- Peng, Y., Lilly, S. J., Kovač, K., et al. 2010, *ApJ*, **721**, 193
- Pipino, A., & Matteucci, F. 2004, *MNRAS*, **347**, 968
- Poggianti, B. M., Moretti, A., Calvi, R., et al. 2013, *ApJ*, **777**, 125
- Ragone-Figueroa, C., & Granato, G. L. 2011, *MNRAS*, **414**, 3690
- Rutkowski, M. J., Cohen, S. H., Kaviraj, S., et al. 2012, *ApJS*, **199**, 4
- Ryan, R. E. 2008, *ApJ*, **678**, 751
- Ryan, R. E., McCarthy, P. J., Cohen, S. H., et al. 2012, *ApJ*, **749**, 53
- Salim, S., Fang, J. J., Rich, R. M., et al. 2012, *ApJ*, **755**, 105
- Scarlata, C., Carollo, C. M., Lilly, S. J., et al. 2007, *ApJS*, **172**, 494
- Schawinski, K., Lintott, C. J., Thomas, D., et al. 2009, *ApJ*, **690**, 1672
- Schawinski, K., Urry, C. M., Simmons, B. D., et al. 2014, *MNRAS*, **440**, 889
- Schiminovich, D. A., Wyder, T. K., Martin, D. C., et al. 2007, *ApJS*, **173**, 315
- Scoville, N., Aussel, H., Brusa, M., et al. 2007, *ApJS*, **172**, 1
- Serra, P., Oosterloo, T., Morganti, R., et al. 2012, *MNRAS*, **422**, 1835
- Sérsic, J. L. 1968, *Atlas de Galaxias Australes* (Cordoba: Observatorio Astronómico)
- Shen, S., Mo, H. J., White, S. D. M., et al. 2003, *MNRAS*, **343**, 978
- Silk, J., & Rees, M. 1998, *A&A*, **331**, L1
- Sonnenfeld, A., Nipoti, C., & Treu, T. 2014, *ApJ*, **786**, 89
- Suh, H., Jeong, H., Oh, K., et al. 2010, *ApJS*, **187**, 374
- Tal, T., van Dokkum, P. G., Franx, M., et al. 2013, *ApJ*, **769**, 31
- Thomas, D., Greggio, L., & Bender, R. 1999, *MNRAS*, **302**, 537
- Thomas, D., Maraston, C., Bender, R., & Mendes de Oliveira, C. 2005, *ApJ*, **621**, 673
- Trager, S. C., Faber, S. M., Worthey, G., & González, J. J. 2000, *AJ*, **119**, 1645
- Trager, S. C., Worthey, G., Faber, S. M., Burstein, D., & González, J. J. 1998, *ApJS*, **116**, 1
- Trujillo, I., Förster Schreiber, N. M., Rudnick, G., et al. 2006, *ApJ*, **650**, 18
- van der Wel, A., Rix, H.-W., Wuyts, S., et al. 2011, *ApJ*, **730**, 38
- van Dokkum, P. G., & Conroy, C. 2010, *Natur*, **468**, 940
- van Dokkum, P. G., Franx, M., Kriek, M., et al. 2008, *ApJL*, **677**, L5
- Vanzella, E., Cristiani, S., Dickinson, M., et al. 2008, *A&A*, **478**, 83
- Williams, C., Giavalisco, M., Cassata, P., et al. 2014, *ApJ*, **780**, 1
- Williams, R., Quadri, R. F., Franx, M., et al. 2010, *ApJ*, **713**, 738
- Windhorst, R. A., Cohen, S. H., Hathi, N. P., et al. 2011, *ApJS*, **193**, 27
- Wuyts, S., Cox, T. J., Hayward, C. C., et al. 2010, *ApJ*, **722**, 1666
- Wyder, K., Martin, D. C., Schiminovich, D., et al. 2007, *ApJS*, **173**, 293
- Yi, S. K., Demarque, P., & Oemler, A., Jr. 1998, *ApJ*, **492**, 480
- Yi, S. K., Kim, Y., & Demarque, P. 2003, *ApJS*, **144**, 259
- Yi, S. K., Lee, J., Sheen, Y.-K., et al. 2011, *ApJS*, **195**, 22
- Yi, S. K., Lee, Y.-W., Woo, J.-H., et al. 1999, *ApJ*, **513**, 128
- Yi, S. K., Yoon, S.-J., Kaviraj, S., et al. 2005, *ApJS*, **619**, L111